

Do Loop Current Eddies stimulate productivity in the Gulf of Mexico?

Pierre Damien^(1,2), Julio Sheinbaum⁽¹⁾, Orens Pasqueron de Fommervault⁽¹⁾, Julien Jouanno⁽³⁾, Lorena Linacre⁽⁴⁾, Olaf Duteil⁽⁵⁾

⁽¹⁾ Departamento de Oceanografía Física, Centro de Investigación Científica y de Educación Superior de, Ensenada, México,

⁽²⁾ University of California, Los Angeles, CA

⁽³⁾ LEGOS, Université de Toulouse, IRD, CNRS, CNES, UPS, Toulouse, France,

⁽⁴⁾ Departamento de Oceanografía Biológica, Centro de Investigación Científica y de Educación Superior de Ensenada, México,

⁽⁵⁾ GEOMAR Helmholtz Centre for Ocean Research, Kiel, Germany.

Corresponding author: Pierre Damien (pdamien@ucla.edu)

Key Points :

- LCEs trigger a local phytoplankton biomass increase in winter.
- Chlorophyll variability at surface does not reflect the seasonal cycle of the depth-integrated biomass.
- Convective mixing and Ekman pumping are key mechanisms to preferentially supply nutrient toward the euphotic layer in LCEs.

18 **Abstract**

19 Surface chlorophyll concentrations inferred from satellite images suggest a strong influence of
20 the mesoscale activity on biogeochemical variability within the oligotrophic regions of the Gulf of
21 Mexico (GoM). More specifically, long-living anticyclonic Loop Current Eddies (LCEs) are shed
22 episodically from the Yucatan Channel Loop Current and propagate westward. This study addresses the
23 biogeochemical response of the LCEs to seasonal forcing and show their role in driving phytoplankton
24 biomass distribution in the GoM. ~~Using an eddy resolving (1/12°) interannual regional simulation~~
25 ~~based on the coupled physical-biogeochemical model NEMO-PISCES that yields a realistic~~
26 ~~representation of the surface chlorophyll distribution, it is shown that the LCEs foster a large biomass~~
27 ~~increase in winter in the upper ocean.~~ Using an eddy resolving (1/12°) interannual regional simulation,
28 it is shown that the LCEs foster a large biomass increase in winter in the upper ocean. It is based on
29 the coupled physical-biogeochemical model NEMO-PISCES that yields a realistic representation of the
30 surface chlorophyll distribution. The primary production in the LCEs is larger than the average rate in
31 the surrounding open waters of the GoM. This behavior cannot be directly identified from surface
32 chlorophyll distribution alone since LCEs are associated with a negative surface chlorophyll anomaly
33 all year long. This anomalous biomass increase in the LCEs is explained by the mixed-layer response
34 to winter convective mixing that reaches deeper and nutrient-rich waters.

35 **I/ Introduction**

36 Historical satellite ocean color observations of the deep waters of the Gulf of Mexico (roughly
37 delimited by the 200m isobath and from hereafter referred to as GoM open-waters) indicate low surface
38 chlorophyll concentrations ([CHL]), low biomass and low primary productivity (Müller-Karger et al.,
39 1991; Biggs and Ressler, 2001; Salmerón-García et al., 2011). The GoM open-waters are mostly
40 oligotrophic, as confirmed by more recent bio-optical in-situ measurements from autonomous floats
41 (Green et al., 2014; Pasqueron de Fommervault et al., 2017; Damien et al., 2018). The surface
42 chlorophyll concentration in the GoM open-waters exhibits a clear seasonal cycle which is primarily
43 triggered by the seasonal variation of the mixed layer depth (Müller-Karger et al., 2015) and river
44 discharges (Brokaw et al., 2019). In tandem, the seasonal cycle is strongly modulated by the energetic
45 mesoscale dynamic activity which shapes the distribution of biogeochemical properties (Biggs and
46 Ressler, 2001; Pasqueron de Fommervault et al., 2017). This mesoscale activity is dominated by the
47 large and long-living Loop Currents Eddies (LCEs) which are shed episodically by the Loop Current
48 (Weisberg and Liu, 2017) and constitute the most energetic circulation features in the GoM
49 (Sheinbaum et al., 2016; Sturges & Leben, 2000).

50 Mesoscale activity (see McGillicuddy et al., 2016 for a review) modulates the phytoplankton
51 biomass distribution (Siegel et al., 1999; Doney et al., 2003; Gaube et al., 2014; Mahadevan, 2014) and
52 the ecosystem functioning (McGillicuddy et al., 1998, Oschlies and Garcon, 1998, Garcon et al., 2001).
53 Specifically, the ability of the mesoscale eddies to enhance vertical fluxes of nutrients is determinant in
54 sustaining the observed phytoplankton growth rate in oligotrophic regions such as the GoM open-
55 waters, where the phytoplankton primary production is limited by nutrient availability in the euphotic
56 layer (McGillicuddy and Robinson 1997; McGillicuddy et al., 1998; Oschlies and Garcon, 1998).

57 The upward doming of isopycnals in cyclonic eddies and downward depressions in anticyclonic
58 eddies, also known as “eddy-pumping”, occur when the eddies are strengthening (Siegel et al., 1999,
59 Klein and Lapeyre, 2009) and produce a nutrient vertical nutrient transport. This has been historically
60 proposed as the dominant mechanism controlling the mesoscale biogeochemical variability, as it
61 induces a reduction of productivity in the anticyclone and an increase in cyclones. This paradigm is
62 however challenged by observations of enhanced surface chlorophyll concentrations in anticyclonic
63 eddies (Gaube et al., 2014), particularly during winter (Dufois et al., 2016). As a plausible explanation,
64 eddy-wind interactions may significantly modulate vertical fluxes through Ekman transport divergence
65 within the eddies (Martin and Richards, 2001, Gaube et al., 2013, 2015). This mechanism is
66 responsible for a downwelling in the core of cyclones and an upwelling in the core of anticyclones.
67 Dufois et al. (2014, 2016) link these observations to a deeper mixed layer in anticyclonic eddies. This is
68 explained by the eddy-driven modulation of the upper ocean stratification which directly affects the
69 winter convective mixing (He et al., 2017). Observed mixed layers tend to be deeper in anticyclones
70 than in cyclones (Williams, 1998; Kouketsu et al., 2012) and vertical nutrient fluxes to the euphotic
71 layer are potentially enhanced in anticyclones during periods prone to convection (e.g. winter in the
72 GoM). Although some consensus exists on the fundamental role of anticyclonic eddies on the
73 productivity of oligotrophic ocean regions, large uncertainties remain regarding the relative importance
74 of the different mechanisms involved in the biogeochemical responses.

75 Besides, in-situ measurements in oligotrophic regions have shown that the surface [CHL]
76 variability, observed from ocean color satellite imagery, is not necessarily representative of the total
77 phytoplankton (carbon) biomass variability in the water column (Siegel et al., 2013; Mignot et al.,
78 2014). In particular, a surface [CHL] winter increase, may result from physiological mechanisms (i.e.
79 modification of the ratio of [CHL] to phytoplankton carbon biomass) or from a vertical redistribution
80 of the phytoplankton (Mayot et al., 2017) rather than from changes in the biomass content. It is not

78 clear yet which of these hypotheses holds in oligotrophic regions, and more specifically in the GoM
79 open-waters where this issue has been addressed by in-situ sub-surface [CHL] observations (Pasqueron
80 de Fommervault et al., 2017). Most of the studies focusing on chlorophyll variability use surface (or
81 near-surface) [CHL] as a proxy for phytoplankton biomass and interpret a [CHL] increase as an
82 effective biomass production. Only a few studies considered the vertically integrated responses (Dufois
83 et al., 2017; Guo et al., 2017; Huang and Xu, 2018) emphasizing the importance of considering the
84 eddy impact on the subsurface.

85 The objective of this study is to better understand the role of LCEs in driving [CHL] distribution
86 and variability within the GoM open-waters. Material and methods used in this study are presented in
87 section 2. In section 3, the imprint of the LCEs on the surface [CHL] distribution is inferred from
88 satellite ocean color observations. Since these measurements are confined to the oceanic surface layer
89 and do not allow access to the vertical properties of LCEs, we complete the analysis with a coupled
90 physical-biogeochemical simulation (subsections 2 and 3). Particular attention is paid to the validation
91 of the modeled LCE dynamical structures and surface [CHL] anomalies. In the last section, we propose
92 to disentangle the mesoscale mechanisms controlling the seasonal cycle of the [CHL] vertical profile in
93 LCEs. The model also enables to assess both abiotic and biotic processes and physical-biogeochemical
94 interactions that can be difficult to address with in-situ observations only.

95 **II/ Material and methods**

96 **II.1/ The coupled physical-biogeochemical model**

97 The simulation analyzed in this study (referred as GOLFO12-PISCES) has been described and
98 compared with observations in Damien et al. (2018). It relies on a physical-biogeochemical coupled
99 model based on the ocean model NEMO (Nucleus for European Modeling of the Ocean, version 3.6;
100 Madec, 2016) and the biogeochemical model PISCES (Pelagic Interaction Scheme for Carbon and
101 Ecosystem Studies; Aumont and Bopp, 2006; Aumont et al., 2015). The model grid covers the GoM
102 and the western part of the Cayman Sea (Fig 1) with a $1/12^\circ$ horizontal resolution (~ 8.4 km). This
103 allows to resolve scales related to the first baroclinic mode, which is of the order of 30-40 km in the
104 GoM open-waters (e.g., Chelton et al., 1998). The model is forced with realistic open-boundary
105 conditions from the MERCATOR reanalysis GLORYS2V3, high frequency atmospheric forcing based
106 on an ECMWF ERA-interim reanalysis (Brodeau et al., 2010), and freshwater and nutrient-rich
107 discharges from rivers (Dai and Trenberth, 2002). The analysis has been performed using 5-day
108 averaged outputs for a period of 5 years from 2002 to 2007. We refer the reader to Damien et al. (2018)
109 for an extended model and numerical setup descriptions. ~~and a careful validation against observations~~
110 ~~that show the ability of the model to reproduce the main hydrographic and nutrient vertical~~
111 ~~distributions in the GoM.~~ In this previous study, an extensive validation of the modeled properties were
112 carried out , focusing on physical properties that are known to influence primary production and
113 chlorophyll concentration: the mixed layer depth and the depth and slope of the nutricline. A novel
114 aspect was to use in-situ observations collected from autonomous floats and published in Green et al.
115 (2014) and Fommervault et al. (2017) to validate not only the modeled surface chlorophyll
116 concentration but also the chlorophyll vertical profile in the GoM. To be able to reproduce the vertical
117 profile of chlorophyll correctly, the parameters of the biogeochemical model were largely tuned
118 compared to the ones suitable for global simulations (Aumont et al., 2015). The ability of GOLFO12-
119 PISCES to reproduce the main observed features of the GoM was demonstrated, at least at a basin and
120 seasonal scale.

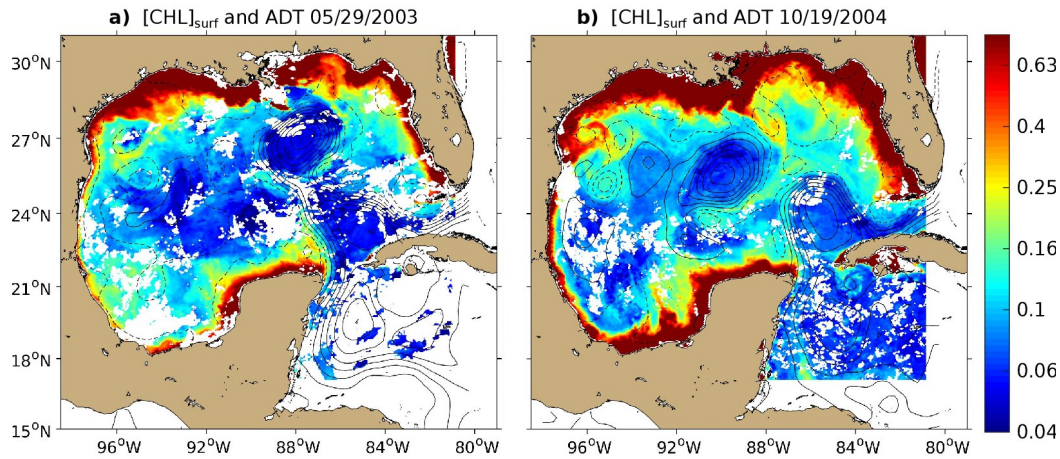


Figure 1: 8-days composite images of $[CHL]_{surf}$ (in $mg \cdot m^{-3}$) around (a) May 29th 2003 and (b) October 19th 2004 derived from Aqua-MODIS images overlaid with contours of Absolute Dynamic Topography (ADT in m) derived from Aviso images are superimposed. Contour interval is 10cm and ADT values lower than 40cm are shown with dashed curves.

II.2/ Observational Data Set Used

Satellite observations are used to evaluate the ability of GOLFO12-PISCES to reproduce the dynamical and biological signatures associated with LCEs. Surface geostrophic velocities are derived from a $1/4^\circ$ multi-satellite merged product of absolute dynamic topography (ADT) provided by AVISO+ (<http://marine.copernicus.eu>). Surface chlorophyll concentrations are from the Aqua-MODIS 4 km product (Sathyendranath et al., 2012; <http://marine.copernicus.eu>) and consist of 8-day composites from 2003 to 2015.

II.3/ LCEs detection, tracking and composite construction

In order to track the LCEs, we use the algorithm developed by Nencioli et al. (2010), which has been extensively employed to track coherent mesoscale eddies (Dong et al., 2012, Ciani et al. 2017,

134 Zhao et al. 2018) and submesoscale eddies (Damien et al., 2017). It is based on the geometric
135 organization of the velocity fields, dominated by rotation, that develop around eddy centers. Here, it is
136 applied to weekly AVISO+ surface geostrophic velocities and GOLFO12-PISCES 5-day averaged
137 velocities at 20m depth. Since LCEs are surface intensified (Cooper et al., 1990; Forristall et al., 1992;
138 Sturges and Kenyon, 2008), the choice of a shallow detection depth is expected to maximize the
139 accuracy. The selection of LCEs is defined using the criteria that eddies have to be shed from the Loop
140 Current.

141 In order to assess the [CHL] response to LCE dynamics, eddy-centric horizontal images and
142 transects of LCEs are used to make composites constructed by averaging modeled variables of the
143 different LCEs collocated to their center. The transect building procedure involves an axisymmetric
144 averaging that assumes axis-symmetry of the dynamical structures and no tilting of their rotation axis.
145 Moreover, we choose not to consider the LCEs formation period and the LCEs destruction period when
146 reaching the western basin (Lipphardt et al., 2008; Hamilton et al., 2018) as LCE destruction/formation
147 involves specific processes (Frolov et al., 2004; Donohue et al., 2016). We therefore focus on the LCEs
148 contained in the central part of the GoM from 86°W to 94°W. Annual composites are computed along
149 with monthly composite averages in order to assess seasonal variability. Composite LCEs averaged
150 during the months of January and February are referred to as winter composites and those averaged
151 during July and August are referred to as summer composites. These composites provide an overview
152 of the LCEs mean hydrographical, biogeochemical and dynamical characteristics.

153 **II.4/ Diagnostics**

154 The LCE radius R_{LCE} is estimated as the radial distance between the center and the peak
 155 azimuthal velocity V_{max} . The mixed layer depth (MLD), a major physical factor influencing nutrient
 156 distribution and [CHL] dynamics (Mann and Lazier, 2006), is defined as the depth at which potential
 157 density exceeds its value at 10m depth by $0.125 \text{ kg} \cdot \text{m}^{-3}$ (Levitus, 1982; Monterey and Levitus, 1997).
 158 An important driver of the mixed layer deepening is the stratification of the water column, which is
 159 evaluated by the square of the buoyancy frequency $N^2(z) = \frac{-g}{\rho_0} \frac{\partial \rho}{\partial z}$, where g is the gravitational
 160 acceleration, z is depth, ρ is density and ρ_0 is a reference density.

161 As carried out in Damien et al. (2018), several metrics are defined and used to describe [CHL]:
 162 • [CHL]_{surf}: [CHL] averaged between 0 and 30 m depth, and considered as surface concentration
 163 (in $\text{mg CHL} \cdot \text{m}^{-3}$),
 164 • [CHL]_{tot}: integrated content of [CHL] over the 0-350 m layer (in $\text{mg CHL} \cdot \text{m}^{-2}$),
 165 • DCM: depth of the Deep Chlorophyll maximum (in m),
 166 • [CHL]_{DCM}: [CHL] value at DCM depth (in $\text{mg CHL} \cdot \text{m}^{-3}$).

167 To understand the mesoscale distribution of [CHL], key biological variables are vertically integrated
 168 between 0 and 350m: the phytoplanktonic concentration [PHY]_{tot}, the primary production rate PP_{tot} and
 169 the grazing rate GRZ_{tot} . PP_{tot} consists of two components: new production PPN_{tot} fueled by nutrients
 170 supplied from a source external to the mixed layer and regenerated production PPR_{tot} sustained by
 171 recycled nutrients within the euphotic layer (Dugdale & Goering, 1967; Eppley & Peterson, 1979),
 172 which depth reaches between 120 and 150 m in the GoM (Jolliff et al., 2008; Linacre et al., 2019). A
 173 normalized chlorophyll concentration anomaly within LCEs, [CHL]', is also computed as
 174 $[CHL]' = [CHL] - \overline{[CHL]}$, where $\overline{[CHL]}$ is the averaged background [CHL] field in the open GoM
 175 waters (for radius > 250km from the LCEs' centers). We also define the normalized anomaly as

176 $[CHL]' / SD([CHL]')$ with SD the standard deviation operator, following a similar approach as
177 Gaube et al. (2013, 2014) and Dufois et al. (2016). To limit the influence of very high [CHL] values in
178 coastal waters under the direct influence of continental discharges, a salinity filtering criterion (lower
179 than 36 psu) is applied. A similar method was used by Gaube et al. (2013, 2014) to filter edge effects
180 but using a distance criterion instead.

181 **III/ Results**

182 **III.1/ Satellite observations of [CHL]**

183 Fig 1 shows the 8-day averaged satellite observations of the surface chlorophyll around May 29th
184 2003 (a) and October 19th 2004 (b). These observations highlight the strong contrast between the
185 eutrophic conditions in the coastal waters and the oligotrophic conditions in the open ocean, as already
186 addressed by several studies (Martinez-Lopez & Zavala-Hidalgo, 2009; Pasqueron de Fommervault et
187 al., 2017). Far from the coast, these figures also reveal that the surface chlorophyll varies at a scale of
188 the order of 100km with a distribution that tends to follow the absolute dynamic topography (ADT)
189 contours.

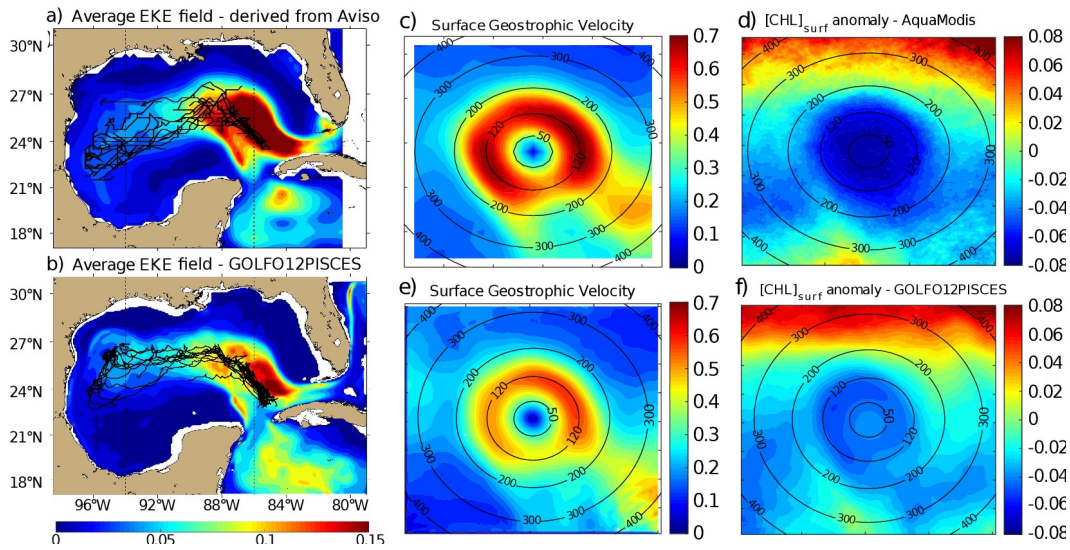


Figure 2: Average eddy kinetic energy (EKE) field derived from (a) Aviso geostrophic surface velocities and from (b) GOLFO12-PISCES currents at 10m depth. The trajectories of the tracked LCEs are superimposed to the EKE field (black lines). Vertical black dashed lines indicate the central GoM area over which composites are built. Annual LCE composite images of surface geostrophic velocities for (c) Aviso images and (e) GOLFO12-PISCES. Annual LCE composite images of surface chlorophyll concentration anomaly for (d) Modis images and (f) GOLFO12-PISCES. Black circles indicate the radius in kilometers.

LCEs trajectories are reported on Fig 2.a, superimposed onto the geostrophic climatological eddy kinetic energy (EKE) field at the surface. EKE is computed from eddy velocities defined on each grid cell as the difference between the total horizontal current and its mean value over 120 days. This time window is chosen to filter the seasonal signal. EKE is concentrated in the LC and on the westward pathway of the LCEs (Lipphardt et al. 2008) demonstrating that LCEs constitute the major source of EKE in the GoM open waters (Sheinbaum et al., 2016; Sturges & Leben, 2000; Hamilton, 2007; Jouanno et al., 2016).

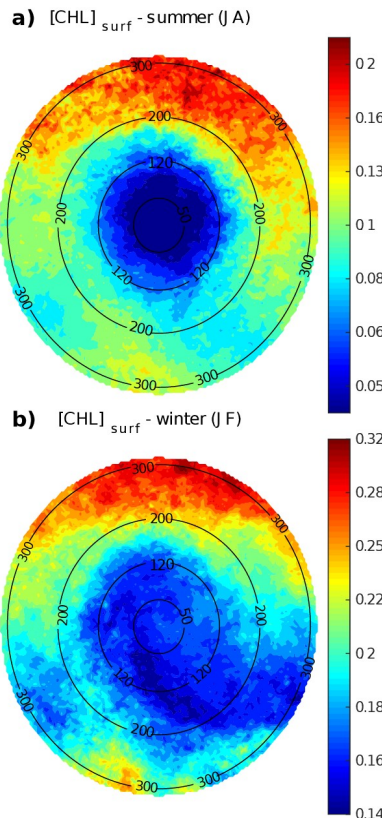


Figure 3: LCE composite images of $[\text{CHL}]_{\text{surf}}$ derived from Aqua-MODIS for the (a) summer and (b) winter seasons. Black circles indicate the radius in kilometers.

LCE annual composites of surface geostrophic velocities (Fig 2.c) and $[\text{CHL}]_{\text{surf}}$ (Fig 2.d) are built from 482 different satellite images. On average, we found that $R_{\text{LCE}} \sim 120$ km and $V_{\text{max}} \sim 0.6\text{-}0.7$ $\text{m}\cdot\text{s}^{-1}$, in agreement with previously reported LCEs (Elliot, 1982; Cooper et al., 1990; Forristal et al., 1992; Glenn and Ebbesmeyer, 1993; Weisberg and Liu, 2017; Tenreiro et al., 2018). LCEs are associated with a negative $[\text{CHL}]_{\text{surf}}$ anomaly (~ -0.07 $\text{mg}\cdot\text{m}^{-3}$ in the annual average). The LCEs influence on $[\text{CHL}]_{\text{surf}}$ is largest in summer (Fig 3.a) when it reaches very low values (< 0.045 $\text{mg}\cdot\text{m}^{-3}$), which corresponds to an anomaly of ~ -0.08 $\text{mg}\cdot\text{m}^{-3}$. This anomaly is less marked-remarkable in winter (~ -0.06 $\text{mg}\cdot\text{m}^{-3}$, Fig 3.b) when $[\text{CHL}]_{\text{surf}} \sim 0.17$ $\text{mg}\cdot\text{m}^{-3}$ within LCEs. The high chlorophyll concentrations in the northern part of the composites (in the southern part too but in smaller proportions) are related to shelves.

III.2/ Dynamical characterization of modeled LCEs

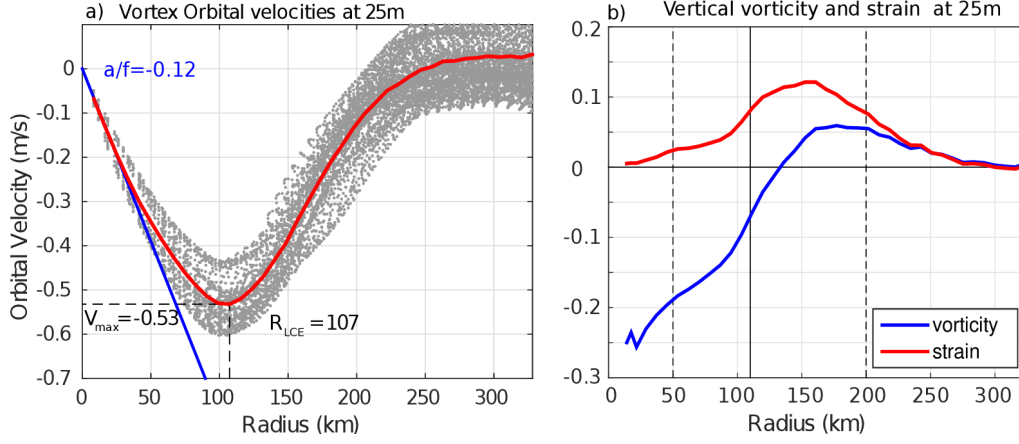
A total of 11 model LCEs were detected during the 5 years of simulation. Their trajectories are reported in Fig 2.b, superimposed upon the climatological EKE field simulated at 10 meters. The westward / southwestward propagation of LCEs is well reproduced (Vukovich, 2007) even though the LCEs translation is almost zonal-westward in GOLFO12-PISCES. Comparison with Fig 2.a shows the ability of GOLFO12-PISCES to represent the mean and transient dynamical features of the GoM open waters (see also see Garcia-Jove et al., 2016).

The robustness of the composite method arises from the number of LCE images used to build the composites:

- Annual composite is built from 605 5-day averaged LCEs pictures-model outputs from 10 different LCEs,
- Summer composite is built from 83 5-day averaged LCEs pictures model outputs from 8 different LCEs,
- Winter composite is built from 93 5-day averaged LCEs pictures-model outputs from 9 different LCEs.

The model LCEs surface geostrophic velocities (Fig 2.e) have important similarities with velocities inferred from altimetry (Fig 2.c) confirming that GOLFO12-PISCES reproduces the surface signature of the LCEs. However, one can also notice an underestimation of the surface orbital velocities ($\sim 25\%$ on average over the 50-200 km radius range). This bias could result from the relatively coarse model resolution and 5-day output frequency that are unable to fully capture the

234 gradient intensity at R_{LCE} . The assumption of an axial symmetry of the LCE circulation around its
 235 center also induces an error that tends to decrease V_{max} .



236 **Figure 4: (a) Orbital velocities at 25m depth in function of the radius of each detected LCE (light gray dots). The red line is the**
 237 **LCE orbital velocity profile of the annually-averaged composite. (b) Vertical vorticity and strain computed from the averaged**

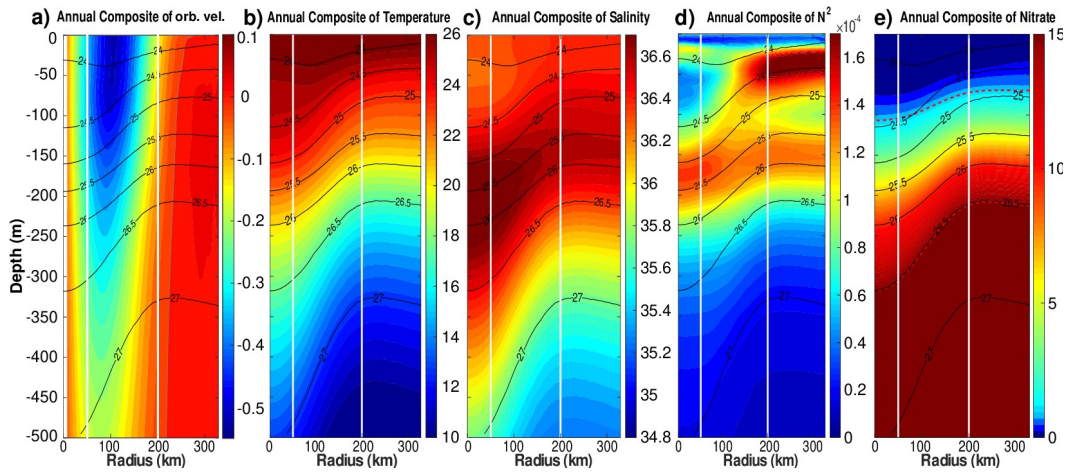
238 **orbital velocity profile assuming no radial velocity in cylindrical coordinates as $\xi_z = \frac{1}{f} \frac{\partial rv}{\partial r}$ and $S = \frac{1}{f} (\frac{\partial v}{\partial r} - \frac{v}{r})$.**

239 Orbital velocities of composite eddies are used to distinguish different dynamical areas within
 240 LCEs. The model annual average dynamical profile at 25m depth (Fig 4) reveals a typical vortex-like
 241 structure with $R_{LCE} \sim 107$ km and $V_{max} \sim 0.53 \text{ m}\cdot\text{s}^{-1}$ and suggests the following decomposition:

- 242 • $r < 50$ km : the **LCEs core**, where the eddy is approximately in solid body rotation: $V_{orb} = a \cdot r$
 243 where the coefficient a is related to the Rossby number ($Ro = 2a/f$). The ratio a/f is estimated
 244 to be ~ -0.12 (Fig. 4). In this field, the strain is reduced to a minimum and the flow is dominated
 245 by rotation.
- 246 • $50 \text{ km} < r < 200$ km: the **LCEs ring** structure where the orbital velocity reaches its maximum
 247 at R_{LCE} and then decreases. The horizontal strain is important in this field, even dominating
 248 vorticity from radius exceeding R_{LCE} .

249 • **R_r** > 200 km: the **background GoM**, where the velocity anomalies related to the LCE vanish.

250 In the vertical (Fig 5.a), LCEs are near-surface intensified anticyclonic vortex rings. At depth,
 251 the orbital peak velocity decreases rapidly. At 500 m depth, $V_{\max} \sim 0.17 \text{ m}\cdot\text{s}^{-1}$ and $R_{\text{LCE}} \sim 75 \text{ km}$, and
 252 the dynamical LCE signal nearly vanishes below 1500 m depth ($V_{\max} < 0.03 \text{ m}\cdot\text{s}^{-1}$). The proposed
 253 division into 3 distinct dynamical regions applies from the surface down to 500 m depth (Fig 5.a).



254 **Figure 5: Annually-averaged LCE composite transects of (a) orbital velocities [m/s], (b) potential temperature [°C], (c) salinity**
 255 **[psu], (d) squared Brunt-Väisälä frequency (N^2 in s^{-2}) and (e) nitrate concentration [$\text{mmol}\cdot\text{m}^{-3}$]. Isopycnals anomalies (black**
 256 **contours) are superimposed on all panels. Vertical white lines delimit the three dynamical fields of the LCE composite. On panel**
 257 **e, dashed red lines highlights two specific iso-nitrate contours: 1 and 15 $\text{mmol}\cdot\text{m}^{-3}$.**

258 The composite hydrological structure of modeled LCEs is shown in Fig 5.b and 5.c. The
 259 depression of isopycnals, associated with a depression of isotherms and isohalines, is characteristic of
 260 oceanic anticyclones. In the core of the eddies, the composite depicts a salinity maximum located
 261 between 100 and 300 m, corresponding to the signature of the Atlantic Subtropical UnderWater
 262 (ASTUW) of Caribbean origin entering the GoM through the Yucatan Channel (Badan et al., 2005;
 263 Hernandez-Guerra & Joyce, 2000; Wuust, 1964). This salinity maximum is not limited to the core of
 264 the LCE but gradually erodes and shallows: 36.82 psu at 200 m in the LCEs core and 36.61 psu at 150

265 m in the background GoM common water. Details on the fate of this salinity maximum investigated
266 with GOLFO12 simulations can be found in Sosa-Gutiérrez et al. (2020). The ASTUW layer (salinity >
267 36.5 psu) is also thicker in the LCEs core (~190 m thick) compared to the background GoM water
268 (~120 m thick). Overall, GOLFO12-PISCES reproduces the observed hydrological structure of LCEs
269 (Elliott, 1982; LeHenaff et al., 2012; Hamilton et al., 2018; Meunier et al., 2018b).

270 The annually averaged LCE composite presents a lens-shaped structure exhibiting a ~50 m thick
271 layer of weakly stratified waters located between 50 and 100 m depth (Fig 5.d). This subsurface modal
272 water presents hydrological characteristics close to the observed background GoM waters (potential
273 temperature ~25.4°C and salinity ~ 36.3 psu, Meunier et al., 2018b) and is surrounded below and above
274 by well stratified layers (Meunier et al., 2018a). The upper pycnocline varies seasonally and vanishes in
275 winter due to the deepening of the mixed layer, whereas the lower pycnocline is permanent.

276 The downward displacement of isopycnals is associated with a depletion of nutrients in the upper
277 layer of the LCEs core (Fig 5.e). This is a typical feature of mesoscale anticyclones in the ocean
278 (McGillicuddy et al. 1998; Oschlies and Garcon, 1998). The 1 mmol.m⁻³ iso-nitrate concentration
279 (hereafter Z_{NO_3} , sometimes referred to as the nitracline as in Cullen & Eppley, 1981; Pasqueron de
280 Fommervault et al., 2017 or Damien et al., 2018) is located at ~ 70 m depth in the background GoM
281 waters whereas it is found much deeper in the core ($Z_{NO_3} \sim 106$ m). At depth, iso-nitrate layers and
282 isopycnals are well correlated (Ascani et al., 2013; Omand & Mahadevan, 2014). For instance, iso-
283 nitrate concentration of 15 mmol·m⁻³ follows the displacements of the 1026.5 kg·m⁻³ isopycnal.
284 However, above 150 m, the density/nitrate relation is different inside and outside the eddies (Z_{NO_3} is
285 collocated with isopycnal 1024.4 kg·m⁻³ in the LCEs core while it is on isopycnal 1024.9 kg·m⁻³ in the
286 background GoM).

III.3/ Surface and vertical distribution of chlorophyll in LCEs

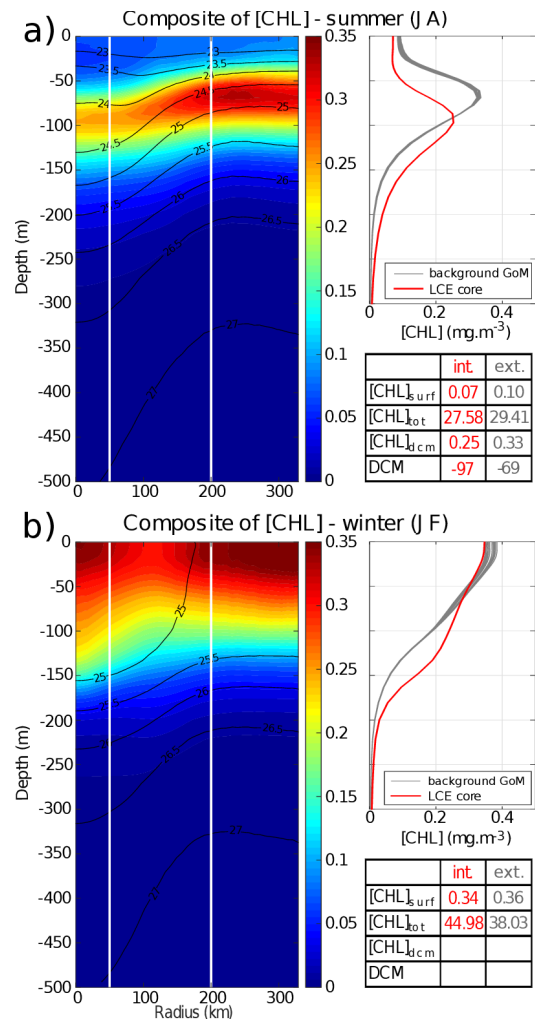


Figure 6: LCE composite transects of [CHL] during summer season (A) and winter season (B). Density anomalies (black contours) are superimposed. Vertical white lines delimit the three dynamical fields of the LCE composite. For each season, [CHL] profiles in the LCE core ($r < 50$ km, red lines) and in the background GoM ($200 \text{ km} < r < 330$ km, gray lines) are plotted. Key metrics concerning [CHL] profiles are also indicated in the tables.

The large difference in stratification between the LCEs core and background GoM suggests a contrasted seasonal response of the [CHL]. This is evidenced by $[\text{CHL}]_{\text{surf}}$ observation (Fig 2.d), with a good model agreement (Fig. 2.f), and is confirmed by the analysis of summer and winter composites of [CHL] vertical distribution:

- In summer (Fig 6.a), $[\text{CHL}]_{\text{surf}}$ is $\sim 30\%$ lower in the LCEs core ($r < 50\text{km}$) than in the background GoM ($200\text{ km} < r < 330\text{ km}$). A pronounced DCM, characteristic of oligotrophic environments, is deeper in the core ($\sim 97\text{ m}$) than in the background GoM ($\sim 69\text{ m}$) with chlorophyll concentrations significantly lower in the interior ($\sim -25\%$).
- In winter, the $[\text{CHL}]$ is maximum at the surface in all the composite domains (Fig 6.b). $[\text{CHL}]_{\text{surf}}$ is lower in the LCEs core compared to the background GoM but the difference is less marked ($\sim -6\%$) than in summer. The main discrepancy is the depth of the inflection point of these profiles. It is deeper in the LCEs core ($\sim 150\text{ m}$), resulting in a more homogenized $[\text{CHL}]$ over a deeper layer than in the background GoM ($\sim 120\text{ m}$).

However, despite reduced surface concentration both in winter and summer, the integrated chlorophyll content, $[\text{CHL}]_{\text{tot}}$, shows a distinct seasonal pattern compared to the surface (tables in Fig 6):

- In summer, $[\text{CHL}]_{\text{tot}}$ is lower in the LCEs core ($27.58\text{ mg}\cdot\text{m}^{-2}$) compared to the background GoM ($29.41\text{ mg}\cdot\text{m}^{-2}$) and $\Delta[\text{CHL}]_{\text{tot}} = -1.83\text{ mg}\cdot\text{m}^{-2}$,
- In winter, $[\text{CHL}]_{\text{tot}}$ is higher in the LCEs core ($44.98\text{ mg}\cdot\text{m}^{-2}$) compared to the background GoM ($38.03\text{ mg}\cdot\text{m}^{-2}$) and $\Delta[\text{CHL}]_{\text{tot}} = +6.95\text{ mg}\cdot\text{m}^{-2}$.

The winter increase of $[\text{CHL}]_{\text{tot}}$ is around 29% in the background GoM whereas it reaches 63% in the LCEs core, leading to $[\text{CHL}]_{\text{tot}}$ in the core being larger than $[\text{CHL}]_{\text{tot}}$ in the background GoM in winter. Meanwhile, $[\text{CHL}]_{\text{surf}}$ remains lower within the LCEs core. The fact that the $[\text{CHL}]$ at the surface does not reflect its depth-integrated behavior means that the peculiar variability of $[\text{CHL}]$ within LCEs may not be fully captured by ocean color satellite measurements. This is consistent with Pasqueron de Fommervault et al. (2017) and Damien et al. (2018) observations and modeling results which addressed the vertical $[\text{CHL}]$ distribution in the GoM.

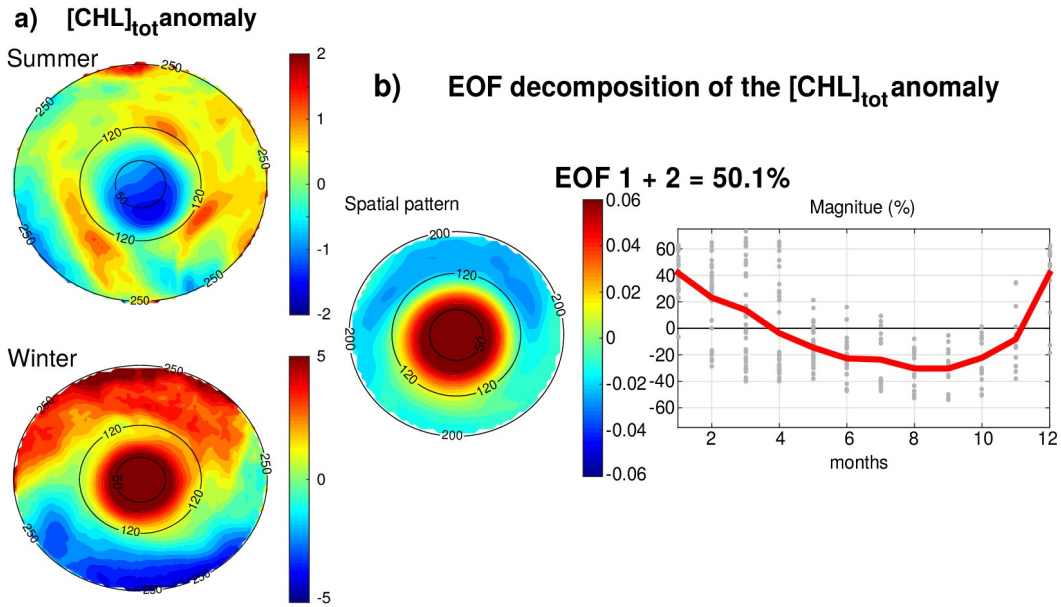


Figure 7: (a) Anomaly of $[CHL]_{tot}$ in summer and winter seasons. Black circles indicate the radius in kilometers. (b) EOF decomposition of the **normalized** $[CHL]_{tot}$ anomaly. The spatial patterns and monthly magnitude (gray dots; the red line represents their monthly averaged value) of the two first modes are indicated. Modes 1 and 2 were summed together (upper panel) and represent 50.1% of the total variance.

$[CHL]_{tot}$ is strongly shaped by both the seasonal variability and the LCEs. The seasonal composites of $[CHL]_{tot}$, shown in Fig 7.a, confirm the summer/winter contrast and highlight a monopole structure with a relatively homogeneous distribution of $[CHL]_{tot}$ within the eddy's core. In order to better characterize the spatio-temporal variability of $[CHL]_{tot}$ induced by LCEs, an Empirical Orthogonal Function (EOF) analysis was performed on the **normalized** $[CHL]_{tot}$ anomaly (Fig 7.b) following the methodology of Dufois et al. (2016). It consists in decomposing the signal into orthogonal modes of variability. Here, we **have chosen choose** to focus on the first two most significant modes which explain 40.2% and 9.9% of the variability. Since they both depict a similar monopole structure in the LCEs core, they were added up in a mode referred to EOF 1+2 responsible for 50% of the total $[CHL]_{tot}$ variance within LCEs. The third eigenmode (not shown) accounts for 6.2% and depicts a dipole structure with opposite polarity located at the east and north of the eddy center. On

average, the EOF1+2 mode is positive in winter (from December to March) and negative the rest of the year (from April to November), with a maximum in January December and a minimum in September. This justifies, a posteriori, the choice to consider winter and summer LCE composites.

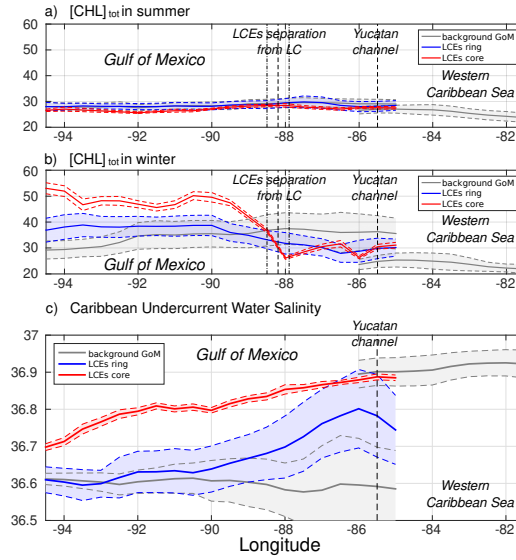


Figure 8: (a) Summer $[CHL]_{tot}$, (b) winter $[CHL]_{tot}$ and (c) salinity of Caribbean waters (ASTUW defined as the subsurface salinity maximum) as a function of longitude in (red) the LCEs core, (blue) the LCEs ring and in (gray) the background GoM. Full lines indicate the averaged value and dashed lines the \pm one standard deviation interval.

The composite evolution of the LCEs $[CHL]_{tot}$ along their westward journey is shown in Fig 8.a and 8.b. It illustrates how the total chlorophyll concentration is preferentially increased in winter within the LCEs core, as soon as the LCEs are shed from the LC. The winter $[CHL]_{tot}$ within LCEs is much larger (exceeding one standard deviation) than the background winter $[CHL]_{tot}$. In terms of integrated $[CHL]$, the LCEs-induced seasonal variability overwhelms the GoM open-waters background seasonal variability.

IV/ Discussion

347 In an oligotrophic environment such as the GoM open-waters, the primary production is
348 generally limited by nutrient supply and $[\text{CHL}]_{\text{tot}}$ exhibits low seasonal variability at the GoM basin
349 scale (Pasqueron de Fommervault et al., 2017). The winter increase of $[\text{CHL}]_{\text{tot}}$ within the LCEs core
350 (which translates into an effective increase of biomass, see appendix A) contrasts and may have large
351 implications for the regional biogeochemical cycles and ecosystem structuration. It also echoes several
352 studies which report elevated $[\text{CHL}]_{\text{surf}}$ within anticyclonic eddies in the oligotrophic subtropical gyre
353 of the southeastern Indian Ocean (Martin and Richards, 2001; Waite et al., 2007; Gaube et al., 2013;
354 Dufois et al., 2016, 2017; He et al., 2017), questioning the classical paradigm of low productivity
355 usually associated with anticyclonic eddies.

356 The mechanisms explaining the LCE impact on $[\text{CHL}]$ are discussed below, trying to rationalize
357 the respective role of abiotic (e.g., trapping, winter mixing, Ekman pumping) and biotic processes (e.g.,
358 primary production (PP), grazing pressure, regenerated versus new PP).

359 **IV.1 Eddy trapping**

360 The distinct hydrological and biogeochemical properties associated with the LCEs core suggest
361 their ability to trap and transport oceanic properties. This mechanism, known as the eddy-trapping
362 (Early et al., 2011; Lehahn et al., 2011; McGillicuddy, 2015; Gaube et al., 2017), is efficient only if the
363 orbital velocities of the vortex are faster than the eddy propagation speed (Flierl, 1981; d'Ovidio et al.,
364 2013). The rotational velocities of the model LCEs are $\sim 0.53\text{m}\cdot\text{s}^{-1}$ are one order of magnitude larger
365 than the propagation velocities ($\sim 0.046\text{ m}\cdot\text{s}^{-1}$ on average). This suggests that LCEs might have a

366 certain ability to trap the water masses present in their core with relatively low exchanges with the
367 exterior.

368 Salinity is well-suited to investigate water masses trapped within the LCEs core during their
369 propagation toward the western GoM (Fig 8.c; Sosa-Gutierrez et al., 2020): salinity distribution shows a
370 marked subsurface maximum that ~~it~~ is not affected by biogeochemical processes. In the Western
371 Caribbean Sea, ASTUW is characterized by high salinity (~ 36.9 psu on average) and low standard
372 deviation (< 0.05 psu). The eastern GoM salinity field reveals that most of the ASTUW crosses the
373 Yucatan Channel within the Loop Current. During the formation of LCEs, a significant part of
374 ASTUW is captured into the LCEs core with low alteration of its properties (Fig 5.c and 8.c). Within
375 the LCEs core, the water mass is transported from eastern to the western GoM where its salinity
376 decreases from 36.9 psu to 36.7 psu. Although altered, the ASTUW signature is still clearly detectable
377 in the GoM western boundary. The other part of ASTUW entering the GoM is found in the LCEs ring.
378 Compared to the core, the salinity in the ring is on average lower (~ 36.8 psu in the eastern GoM) and
379 presents a high standard deviation, pointing out that more recent ASTUW co-exists with older ASTUW
380 that yields ~~eroded-lower~~ salinity maxima. As LCEs travel westward across the GoM, salinity in the
381 LCEs ring decays rapidly to reach values similar to the background GoM values (~ 36.6 psu). This
382 homogenization mainly arises from vertical mixing and winter mixed layer convection (Sosa-Gutierrez
383 et al., 2020). Horizontal intrusions and filamentation may also contribute to this homogenization
384 (Meunier et al., 2020). The composites also suggest that almost no ASTUW enters the GoM apart from
385 the LCEs. The slight increase of the background salinity from eastern to western GoM is a consequence
386 of the diffusion of salt from the LCEs toward the exterior.

387 Although LCEs undergo considerable decaying rates, their erosion is particularly strong in the
388 ring while the core remains better isolated from the surrounding waters (Lehahn et al., 2011; Bracco et

al., 2017). Since no significant $[\text{CHL}]_{\text{tot}}$ seasonal variability is reported in the Western Caribbean Sea (Fig. 8), the biogeochemical behavior in the LCEs core has then to be driven by local processes with low influence of horizontal advective process from the ring or of the Caribbean waters trapped during the LCEs formation. Given that the LCEs core is also quite homogeneous, the following discussion relies on the analysis of the seasonal cycles of selected parameters averaged within the LCEs core.

IV.2 Nitracline depth and nutrient supply into the mixed layer

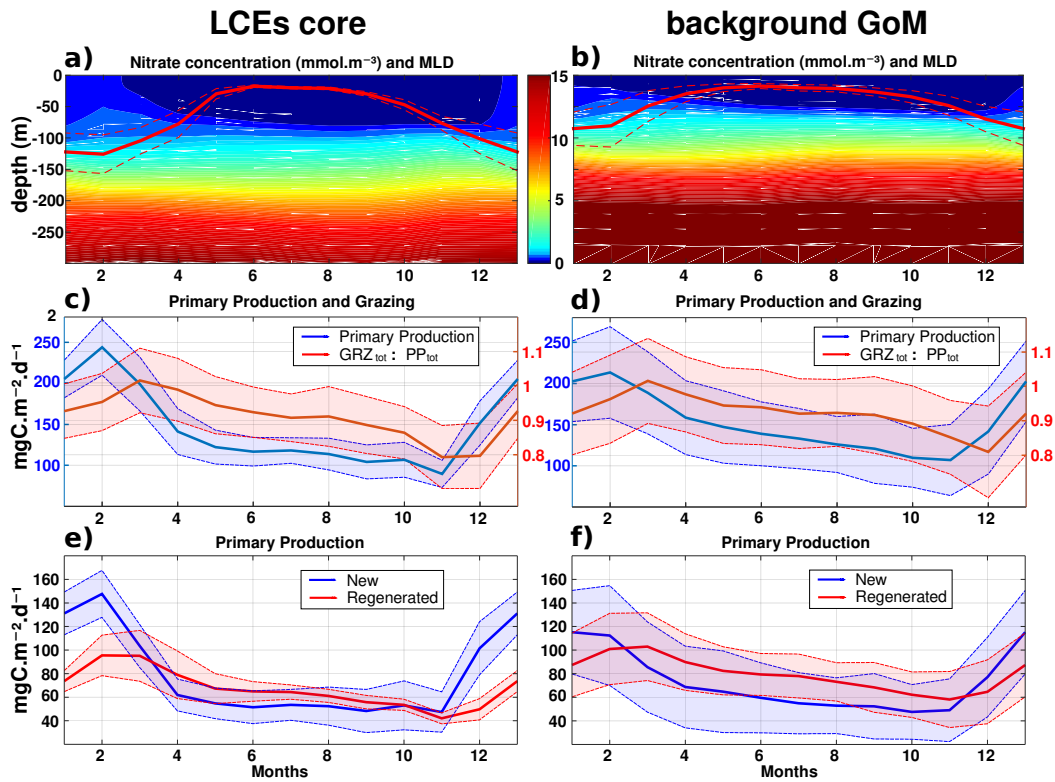


Figure 9: Climatological seasonal cycles of (a and b) nitrate concentration profiles (the red line overlaid is the average mixed layer depth), (c and d) the total primary production (blue) and the ratio of grazing rate over primary production (red) and (e and f) the new (blue) and regenerated (red) primary production. The left panels (a, c and e) refer to the seasonal time series in the LCEs core ($r < 50$ km) whereas the right panels (b, d and f) refer to the seasonal time series in the background GoM ($r > 200$ km). For each average cycle, the mean value is shown (full line) along with its variability (± 1 standard deviation relative to the mean, dashed lines).

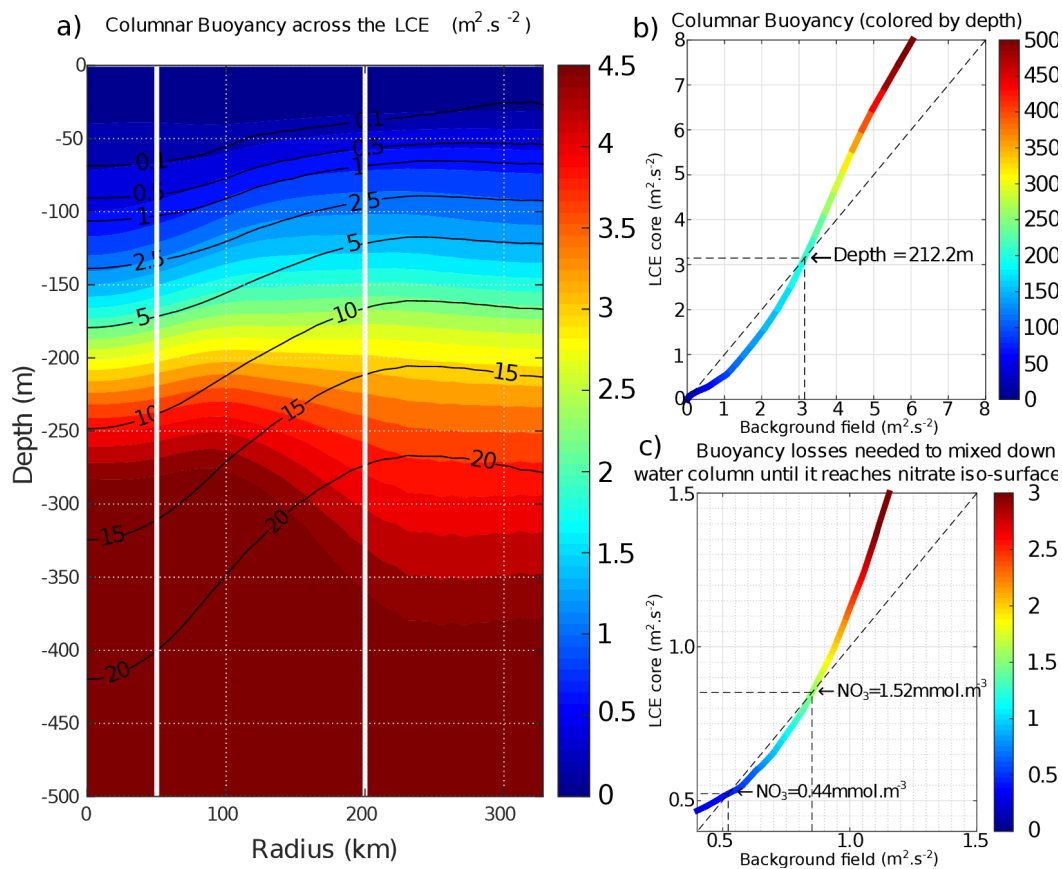
401 The LCEs impact the upper ocean stratification (Fig 5.d), the nutricline depth (Fig 5.e) and
402 consequently the nutrient supply to the euphotic layer (McGillicuddy et al., 2015). The relationship
403 between mixed layer deepening and nutrient supply is studied here by comparing the Z_{NO3} with the
404 MLD (Fig 9.a,b).

405 In late-spring and summer (from May to September), the water column is stratified (shallow
406 MLD) and the downward displacement of the isopycnals within the LCEs pushes nutrients below the
407 euphotic zone (see also Figs 5.e, 6.a): less nutrients are available within the LCE cores for
408 phytoplankton growth, explaining a deeper and less intense DCM. In winter, the convective mixing,
409 fostered both by intense buoyancy losses and strong mechanical energy input at the surface, causes a
410 larger deepening of the mixed layer within the LCEs core (\sim - 125 m, Fig 9.a) compared to the
411 background (\sim - 85 m, Fig 9.b). This asymmetry is due to a pronounced decrease of the surface and
412 subsurface stratification within the LCE core (Fig 5.d, Kouketsu et al., 2012). A quantitative diagnostic

413 of the stratification is given by the columnar buoyancy, $\int_0^H N^2(z) \cdot z \cdot dz$ which measures the buoyancy
414 loss required to mix the water column to a depth H (Herrmann et al. 2008). Fig 10.a reveals significant
415 differences in pre-winter buoyancy between the eddy core and its surroundings. Assuming that the
416 change in buoyancy content is mainly controlled by the buoyancy flux at the surface (see Turner 1973;
417 Lascaratos & Nittis, 1998), it suggests that mixing the water column down to \sim -210 m depth requires
418 smaller surface buoyancy loss in LCEs cores compared to the background GoM (Fig 10.b).

419 However, the larger winter deepening of the mixed layer within the LCEs core is not a sufficient
420 condition to explain a larger nutrient supply. Indeed, it fosters the transport of nutrients from the

421 nitracline toward the mixed layer because both are getting closer. Fig 10.c highlights that a smaller
 422 buoyancy loss mixes down the water column to greater nutrient concentration levels in the LCEs core
 423 compared to the LCEs surrounding. This likely explains the winter increase of surface nitrate
 424 concentration within the LCEs (Fig 9.a). In addition, a diagnostic of the different contributions to
 425 $[\text{NO}_3]$ evolution is proposed in appendix B. It shows the dominant role of vertical advection and
 426 diffusion in winter in providing nutrients to the euphotic layer in the LCEs core.



427 **Figure 10: (a) Columnar Buoyancy transect composite in summer, corresponding to pre-winter mixing season. Iso-nitrate**
 428 **concentrations (black contours) are superimposed. Vertical white lines delimit the three dynamical fields of the LCE composite.**
 429 **(b) Vertical increase of the columnar buoyancy in the LCEs core versus the background GoM. Colors refer to depth. (c)**
 430 **Columnar buoyancy loss required to mix the water column down to the iso-nitrate surface defined by the line color.**

431 So far we have assumed that the surface buoyancy fluxes are identical over the LCEs core and
432 the background GoM. However, this is not strictly the case because temperature/salinity features in the
433 LCEs and background waters are different (Fig 5.b,c; see also Williams 1988). The modeled surface
434 buoyancy loss during winter season is ~18 % more intense within the LCEs. This difference is
435 substantial and probably mainly driven by additional surface cooling applied on the warm LCE core
436 through air-sea interaction. It contributes to enhance convection within the eddies core, and then
437 nutrient supply toward the surface.

438 **IV.3 Productivity and grazing**

439 The primary productivity PP_{tot} presents a clear seasonal cycle both in the LCEs cores and in the
440 background GoM with lower values in October-November, a sharp increase starting in November, a
441 maximum in February and a gradual decrease from March to October (Fig 9.c and 9.d). The pressure
442 exerted by zooplankton grazers varies seasonally. It shows a similar seasonal cycle in the LCEs core
443 and in the background GoM. On average, ~90% of the total daily growth is consumed by grazing,
444 reaching the highest impact in March, just one month after the peak season of the PP_{tot} in both LCEs
445 dynamical areas. The annual PP_{tot} is slightly lower in the LCEs core ($\sim 142.4 \text{ mgC} \cdot \text{m}^{-2} \cdot \text{d}^{-1}$) than in the
446 background GoM ($\sim 148.9 \text{ mgC} \cdot \text{m}^{-2} \cdot \text{d}^{-1}$). The amplitude of the seasonal cycle is larger in the LCEs
447 core: from April to November, PP_{tot} is on average ~12% lower in the LCEs core whereas, in winter,
448 PP_{tot} is ~14% higher where it reaches $\sim 243.2 \text{ mgC} \cdot \text{m}^{-2} \cdot \text{d}^{-1}$ in February. Particularly in the LCE core, the
449 PP_{tot} seasonal cycle is tightly correlated with vertical mixing revealing the important role of mixing in
450 the biogeochemistry. The relatively low standard deviation of the monthly PP_{tot} distribution in the LCE
451 core supports the idea that the influence of the seasonal variability of the forcing largely overwhelms
452 their interannual and sub-monthly variability.

453 The ratio of the PPN_{tot} and PPR_{tot} provides information about the mechanisms controlling the
454 biomass growth (Fig 9.e and 9.f). In winter, the PPN_{tot} plays a leading role, reaching up to 113-147
455 $mgC \cdot m^{-2} \cdot d^{-1}$, driven by the winter mixing and induced NO_3 fluxes (see Appendix B). Conversely, the
456 PPR_{tot} is dominant from April to October. During this period, low NO_3 resources are available in the
457 euphotic layer and the ecosystem preferentially uses ammonium to sustain the PP_{tot} . This seasonal
458 pattern is characteristic of oligotrophic environments such as the GoM open waters (Wawrik et al.,
459 2004; Linacre et al., 2015). In winter, changes in PP_{tot} are correlated to the intensity of winter mixing in
460 the LCEs core (Fig 9.c) and the background GoM (Fig 9.d). The larger PPN_{tot} in the eddy core is
461 consistent with a larger supply of NO_3 and evidences that the core of anticyclones can be preferential
462 spots of enhanced biological production.

463 The pressure exerted by zooplankton grazers varies seasonally (Fig 9.c .d). It shows a similar
464 seasonal cycle in the LCEs core and in the background GoM. On average, $\sim 90\%$ of the total growth is
465 consumed by grazers, reaching the highest impact in March, just one month after the peak season of the
466 PP_{tot} in both areas. In February the difference between the primary production and the grazing rate is
467 larger in the LCEs core than in the GoM background (Fig. 9.c), leading to an enhanced net primary
468 production. Considering the ecosystem from a “top-down” perspective, the grazing rate also
469 participates then in enhancing $[CHL]_{tot}$ within the LCEs core compared to the background.

470 **IV.4 How to explain summer productivity?**

471 In summer, the total primary production is higher in the background GoM waters as the
472 regenerated production rate is higher. Since grazing is known to be a major source of recycled nutrients

473 in the euphotic zone (Sherr and Sherr, 2002), the lower grazing rate inside the LCE during summer
474 (Fig. 9. c. d.) likely explains this lower regenerated production. In addition, production of organic
475 matter occurs in a deeper layer within the LCEs core compared to the background GoM (Fig. B1. e. f.).
476 It is then more likely exported out of the euphotic layer in the form of settling particle, leading to lower
477 remineralization rates in the upper layers to feed regenerated production. More surprising ~~But~~
478 surprisingly, the new primary production exhibits similar rates in both regions, although NO₃ depletion
479 occurs deeper in the LCEs core. In the absence of a strong enough vertical mixing when the mixed
480 layer is shallow, this apparent mismatch requires an additional mechanism, vertical advection, capable
481 to supply NO₃ to the euphotic layer (Sweeney et al., 2003; McGillicuddy et al., 2015).

482 The model vertical velocity in the LCEs reveals an upward pumping in their core (Fig 11). The
483 vertical velocity between 100 and 500 m is on average + 0.07 m·day⁻¹. This vertical transport is mainly
484 driven by two mechanisms, eddy pumping (Falkowski et al., 1991) and eddy-wind interaction (Dewar
485 and Flierl, 1987), but their relative importance is difficult to quantify (Gaube et al. 2014; McGillicuddy
486 et al., 2015).

487 The eddy pumping mechanism is related to the decay of the rotational velocities from the
488 moment LCEs are released from the Loop Current. In the LCE core, this decay is considered as
489 moderate since lateral diffusivity is expected to be relatively low (section V.1). This process may
490 however be considerable in the LCE ring where the erosion rates are important (Meunier et al., 2020).

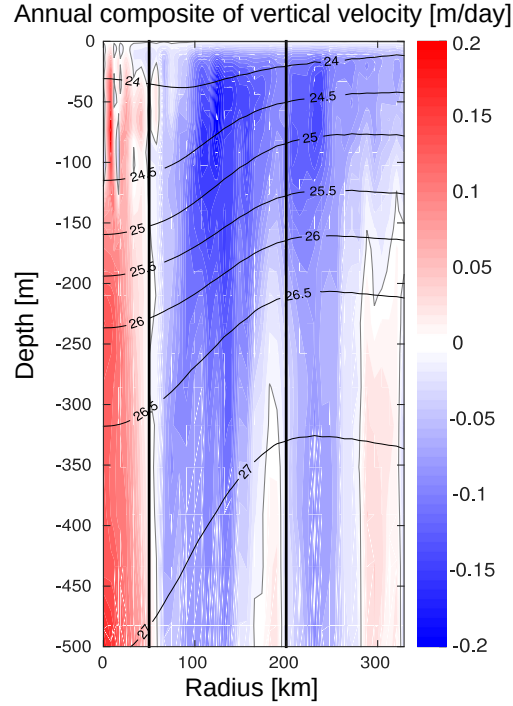


Figure 11: Annually-averaged LCE composite transects of vertical velocities (m/day). Isopycnals anomalies (black contours) are superimposed on all panels. Vertical white lines delimit the three dynamical fields of the LCE composite.

Eddy-wind interactions are due to mesoscale modulation of the Ekman transport. Following the observation of a LCE core in quasi-solid body rotation, the horizontal vorticity varies little with the radius resulting in a negligible “non-linear” contribution of the Ekman pumping (McGillicuddy et al., 2008; Gaube et al., 2015). Assuming a small effect of the eddy SST-induced Ekman pumping, the total

Ekman pumping simplifies into its “linear” contribution computed as $W_E = \frac{\nabla \times \tau}{\rho_0 \cdot (f + \zeta)}$, where ρ_0 is the surface density, f the Coriolis parameter, τ the stress at the sea surface depending on both the wind and ocean currents at the surface (Martin and Richards, 2001, equation 12) and $\nabla \times$ the curl operator. Considering uniform wind velocities ranging from 4.5 to 7.5 m·s⁻¹ (Nowlin & Parker, 1974; Passalacqua et al., 2016) blowing over the LCE, the curl of the stress arises from the anticyclonic surface circulation generated by the eddy. Its manifestation is a persistent horizontal divergence at surface balanced by an upward pumping in the eddy interior (see Martin & Richards, 2001; Gaube et

504 al., 2013, 2014 for further details). With $\rho_0 \sim 1023 \text{ kg}\cdot\text{m}^{-3}$ and $f \sim 6.2\cdot 10^{-5} \text{ s}^{-1}$, we estimate W_E to be in
505 the order of range from $+0.06$ to $0.13 \text{ m}\cdot\text{day}^{-1}$, in agreement with the modeled vertical velocity
506 within the core. The Ekman-eddy pumping mechanism could explain a large fraction of the gradual
507 upwelling of isopycnals within the eddy's core (Fig. 11) and may actively contribute to the advective
508 vertical flux of nutrients (see Appendix B). In summer, this mechanism could explain why new primary
509 production rates are similar in the LCEs core and the background GoM waters although the nutrient
510 pool is located much deeper in the LCEs core.

511 The eddy-Ekman pumping persists in the LCEs core throughout their lifetime as long as there is
512 a wind stress applied at the surface. During wintertime, we expect that both vertical mixing and eddy-
513 Ekman pumping participate to increase the new primary production. A question then arises on the
514 relative contribution of winter mixing to eddy-Ekman pumping in the LCEs core primary production
515 increase in winter. This issue was tackled by He et al. (2017) and Travis et al. (2019) comparing the
516 rate of change of the mixed layer depth with the vertical velocity induced by the eddy-Ekman pumping
517 (equation 4 in He et al, 2017). In the GoM, even if the wind shows larger magnitudes in winter, it is
518 also associated with a large variability. As a consequence, the variability of Ekman pumping is also
519 found large and a robust seasonal seasonal cycle which would allow to isolate the Ekman pumping in
520 winter cannot be clearly identified. However, in the LCEs core, we estimate the mixed layer to deepen
521 at roughly $0.8 \text{ m}\cdot\text{day}^{-1}$, which is on average about 10 times one order of magnitude larger than the
522 higher bound of the estimated pumping mechanism typically occurring in winter in response to stronger
523 wind events. This supports winter mixing as the overwhelming process for the LCEs-induced primary
524 production peak in winter.

525 **V/ Summary and perspectives**

526 The [CHL] variability induced by the mesoscale Loop Current Eddies in the Gulf of Mexico is
527 studied by analyzing vortex composite fields generated from a coupled physical-biogeochemical model
528 at 1/12° horizontal resolution. LCEs are hotspots for mesoscale biogeochemical variability. Despite the
529 [CHL]_{surf} negative anomaly associated with their core ($r < 50$ km), model results indicate that LCEs are
530 associated with enhanced phytoplankton biomass content, particularly in winter. This enhancement
531 results from the contribution of multiple mechanisms of physical-biogeochemical interactions and
532 contrasts with the background oligotrophic surface waters of the GoM.

533 The main results of this study are:

- 534 • LCEs cores present a negative surface chlorophyll anomaly,
- 535 • Unlike [CHL]_{surf}, [CHL]_{tot} is larger in the LCEs cores compared to the background GoM in
536 winter.
- 537 • LCEs core trigger a large phytoplankton biomass increase in winter,
- 538 • The winter mixing is a key mesoscale mechanism that preferentially supplies nutrients to the
539 euphotic layer within the LCEs core. Consequently, it drives an eddy-induced peak of new
540 primary production,
- 541 • Ekman-eddy pumping is a significant mechanism for sustaining relatively high new primary
542 production rates within LCE cores during summer.

543 The phytoplankton biomass increase in individual LCEs cores suggests that LCEs play an important
544 role in sustaining the large-scale GoM productivity.

545 GOLFO12-PISCES provides numerical results which were largely confronted to observations.
546 This extensive validation gives confidence about its ability to produce realistic seasonal and mesoscale
547 variability of biogeochemical tracers at surface and sub-surface, in particular the one associated with

548 LCEs. However, biases are inherent to model and these results exposed in this study would require
549 confirmation by sub-surface in-situ measurements within the core of LCEs.

550 Although the biological response to LCEs may present some specificities due to the particular
551 dynamical nature of LCEs, this study suggests potentially generic insights on the biogeochemical role
552 that anticyclonic eddies could play in oligotrophic environments. It echoes the previous works of
553 Martin and Richards (2001), Gaube et al. (2014, 2015) and especially Dufois et al. (2014, 2016) and He
554 et al. (2017) who proposed winter vertical mixing as an explanation for the positive $[\text{CHL}]_{\text{surf}}$ anomaly
555 observed in anticyclones in the South Indian Ocean. One of the most crucial points to be underlined
556 from our results is that the enhanced primary production and biomass content within anticyclonic
557 eddies may not necessarily be correlated with the surface layer variability. In oligotrophic areas, the
558 integrated content of chlorophyll in the water column has to be considered. This implies that caution
559 should be exercised in the analysis and interpretation of $[\text{CHL}]_{\text{surf}}$ observed by remote sensing
560 instruments and highlights the crucial need for in-situ biogeochemical and bio-optical measurements.
561 In oligotrophic environments, defined by their low production rates and their low chlorophyll
562 concentration, anticyclonic eddies are able to trigger local enhanced biological productivity and
563 generate phytoplankton biomass positive anomalies. In a scenario of expansion of oligotrophic areas
564 (Barnett et al., 2001; Behrenfeld et al., 2006; Polovina et al., 2008), the fate and role of mesoscale
565 anticyclones is an important aspect to be considered.

566 This study focuses on mesoscale physical-biogeochemical interactions which is the spectral
567 range resolved by GOLFO12-PISCES configuration. It evidences the important role of mixing on
568 primary production in the LCE core at seasonal scale. However, mixing also presents significant
569 fluctuations at higher frequencies, associated with particular atmospheric events like storms. The PP_{tot}
570 response to such forcing requires further investigation to verify if the correlation between PP_{tot} and

571 mixing still hold on at higher frequencies where additional other drivers might also become important.
572 ~~To go further into the analysis of anticyclonic eddies in oligotrophic environments,~~ For instance, the
573 role of submesoscale is of particular interest since it has been proved to trigger mechanisms of
574 significance importance for biogeochemistry (Levy et al., 2018). Higher model resolutions can locally
575 enhanced density gradients (Levy et al., 2012; Omand et al., 2015) leading to ageostrophic circulations
576 that perturbs the circular flow around vortices (Martin and Richards, 2001) or enhanced vertical
577 velocities that potentially foster the nutrient supply to the euphotic layer. Beside the mesoscale Ekman
578 pumping located at the eddy center, eddy-wind interactions also produce vertical velocities at the eddy
579 periphery (e.g. Flierl and McGillicuddy, 2002). Finally, it is also worth noting that anticyclonic
580 mesoscales eddies are capable of trapping near-inertial energy waves in the ocean (Kunze 1985,
581 Danioux et al. 2008, Koszalka et al. 2010, Pallas-Sanz et al., 2016) where they produce vertical
582 recirculation patterns (Zhong and Bracco, 2013). Even if, some of these dynamical aspects are partially
583 resolved at 1/12° horizontal resolution, higher resolutions simulations with higher frequency outputs
584 are necessary to correctly assess their specific impact.

585 **Acknowledgments:** Research funded by the National Council of Science and Technology of Mexico –
586 Mexican Ministry of Energy – Hydrocarbon Trust, project 201441. This is a contribution of the Gulf of
587 Mexico Research Consortium (CIGoM). We acknowledge the provision of supercomputing facilities
588 by CICESE.

589 **APPENDIX A: CHL/C-biomass ratio and ecosystem structure**

590 [CHL] is widely used as a proxy for photosynthetic biomass (Strickland, 1965; Cullen, 1982).
591 However, in addition to depend on phytoplankton concentration, it is also affected by several other
592 factors mainly produced by intracellular physiological mechanisms (Geider, 1987). In particular,
593 photoacclimation processes have been proved to be determinant to explain [CHL]_{surf} variability in
594 oligotrophic areas (Mignot et al. 2014). In the GoM open-waters, this issue was specifically addressed
595 at a basin scale in Pasqueron de Fommervault et al. (2017) considering in-situ particulate
596 backscattering measurements and in Damien et al. (2018) from modeling tools. They both reach the
597 same conclusion: [CHL]_{tot} variability provides a reasonably good estimate of the total C-biomass
598 variability ([PHY]_{tot}).

599 This is confirmed by the small amplitude of the seasonal cycle of the ratio [CHL]_{tot}/[PHY]_{tot} in
600 the background GoM (0.256 +/- 0.004 g·mol⁻¹ averaged throughout the year, Fig A1). In the LCEs
601 core, this statement is still valid but must be qualified, since the ratio [CHL]_{tot}/[PHY]_{tot} presents small
602 but significant changes through the year (Fig A1.a). It is around 0.24 g·mol⁻¹ from March to November
603 and increases sharply in December to reach about 0.32 g·mol⁻¹ in January and February. As a result, in
604 winter, the photoacclimation mechanism accounts for ~25% of the total [CHL]_{tot} increase (the
605 remaining part being an effective phytoplankton biomass increase). In summer, the ratio
606 [CHL]_{tot}/[PHY]_{tot} is slightly lower in the LCEs core compared to the background GoM. As a
607 consequence, the [CHL]_{tot} negative anomaly associated with LCEs core does not necessarily translate
608 into a [PHY]_{tot} negative anomaly.

609 Overall in the GoM open-waters, there is a dominance of the small-size phytoplankton over the
610 large-size class in proportion closed to 80%-20% (Linacre et al., 2015). Although the modeled

ecosystem structure is relatively simple, this typical community size structure is well reproduced by GOLFO12-PISCES (Fig A1.c and A1.d), that also suggests a shift in the ecosystem structure in winter. The different response among size classes results from the enhancement of nutrient vertical flux. The role of “secondary” nutrient in this change in the community composition must not be overlooked also, in particular for diatoms (accounted in the model’s large-size group) since they also uptake on silicate (Benitez-Nelson et al., 2007). Moreover, GOLFO12-PISCES exhibits a modulation of the ecosystem structure by LCEs. The dominance of small-size phytoplankton is slightly more marked in summer and the winter shift is stronger in the LCEs core.

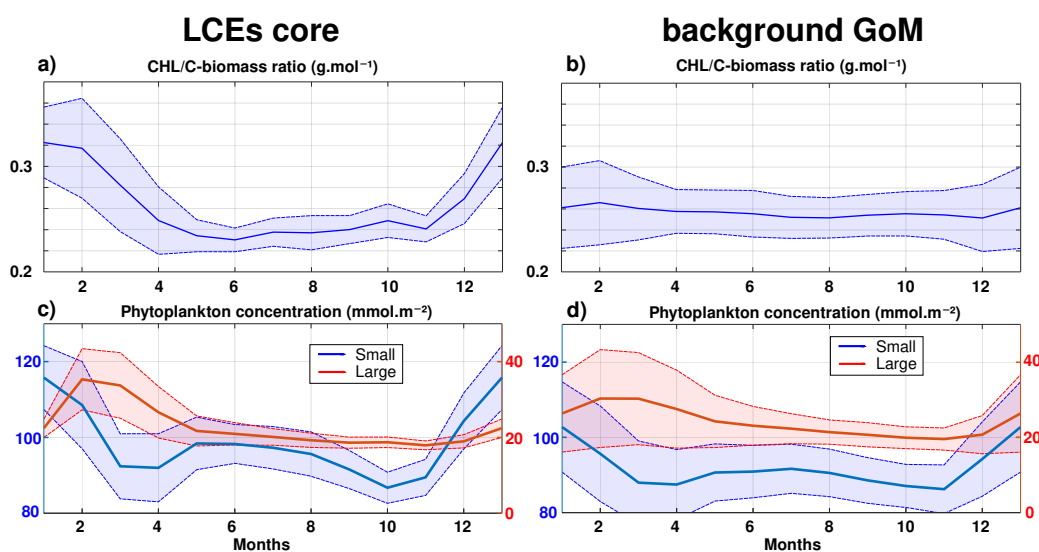


Figure A1: Climatological seasonal cycles of (a and b) the CHL/C-biomass ratio and (c and d) the vertically integrated content of phytoplankton concentration (small size in blue, large size in red). The left panels (a and c) refer to the time series in the LCEs core ($r < 50$ km) whereas the right panels (b and d) refer to the time series in the background GoM ($r > 200$ km). For each average cycle, the average value is shown (full line) along with its variability (± 1 standard deviation relative to the mean, dashed lines).

624 **APPENDIX B : Nitrate budget at a seasonal scale**

625 Nutrients availability in the euphotic layer is a key mechanism to trigger biomass increase in
 626 LCEs. The processes driving the seasonality of nutrient concentrations are here investigated diagnosing
 627 the different contributions to nitrate concentrations (hereafter [NO₃]) variability. The goal is to confirm
 628 the vertical transport of nutrients and quantify the budget in order to determine the driving mechanisms.
 629 The analysis is restricted to nitrate concentrations, considered as the main limiting factor for large size-
 630 class phytoplankton growth in the GoM (Myers et al., 1981; Turner et al., 2006), although phosphates
 631 and silicates are also modeled. We do not exclude that phosphates or silicates could also play a
 632 significant role. In cylindrical coordinates, the [NO₃] equation reads:

633

$$\begin{aligned} \frac{\partial NO_3}{\partial t} = & \underbrace{-V_r \frac{\partial NO_3}{\partial r}}_{\text{radial advection}} - \underbrace{\frac{V_\theta}{r} \frac{\partial NO_3}{\partial \theta}}_{\text{azimuthal advection}} - \underbrace{V_z \frac{\partial NO_3}{\partial z}}_{\text{vertical advection}} + \underbrace{\frac{D_l}{r} \frac{\partial}{\partial r} \left(r \frac{\partial NO_3}{\partial r} \right)}_{\text{lateral diffusion}} + \underbrace{\frac{D_l}{r^2} \frac{\partial^2 NO_3}{\partial \theta^2}}_{\text{lateral diffusion}} \\ & + \underbrace{\frac{\partial}{\partial z} \left(K_z \frac{\partial NO_3}{\partial z} \right)}_{\text{vertical diffusion}} + \underbrace{SMS}_{\text{Source minus sink}} + Asselin \end{aligned}$$

634 Basically, this is a 3D advection-diffusion equation with added "sources and sinks" terms, namely
 635 biogeochemical release and uptake rates. One must include also an "Asselin term", a modeling artifact
 636 due to the Asselin time filtering. We focus on the seasonal cycle of three particular trend terms: the
 637 vertical mixing (Fig B1.a and B1.b), the vertical advection (Fig B1.c and B1.d) and a "source minus
 638 sink" term (Fig B1.e B1.f).

639 [NO₃] variations from vertical dynamics are mainly positive, especially in the first 100 m of the
 640 water column. This traduces in year-round NO₃ source driven by physical processes. By contrast,
 641 biogeochemical processes consume NO₃ in the upper layer to sustain the primary production (Fig B1.e
 642 and B1.f). In the sub-surface layer (~ below the isoline on which nitrate concentration is equal to 2
 643 mmol.m⁻³), the process of nitrification constitutes a biological source of [NO₃]. To first order, this

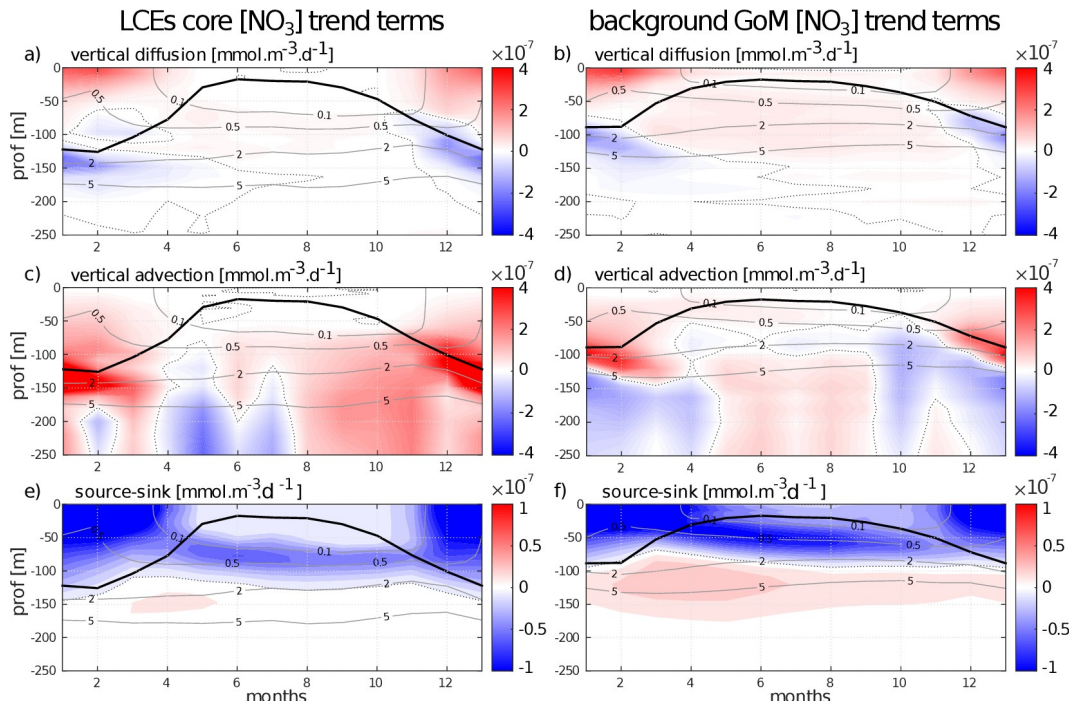
644 represents the global functioning of the ecosystem, valid in both fields and throughout the year.
645 However, the seasonal cycle strongly influence the magnitude of these trend terms, in particular in the
646 LCE core.

647 In winter, from December to February, vertical advective and diffusive motions produce an
648 increase of $[\text{NO}_3]$ within the mixed layer. This tendency consists in an advective entrainment resulting
649 from the deepening of the mixed layer which mainly acts to increase $[\text{NO}_3]$ at the base of the mixed
650 layer (Fig B1.c and B1.d) and vertical mixing which redistributes vertically the nutrients and tends to
651 homogenize $[\text{NO}_3]$ in the mixed layer (Fig B1.a and B1.b). The winter $[\text{NO}_3]$ increase is most important
652 in the LCE core at the base of the mixed layer ($\sim + 6.5 \cdot 10^{-7} \text{ mmol} \cdot \text{m}^{-3} \cdot \text{d}^{-1}$, nearly 3 times larger than in
653 the background GoM), attesting here a preferential NO_3 uplift due to deeper convection. Integrated
654 over the mixed layer, the winter vertical fluxes produce $[\text{NO}_3]$ enhancement of $\sim 2.4 \cdot 10^{-5} \text{ mmol} \cdot \text{m}^{-2} \cdot \text{d}^{-1}$
655 in the eddy core whereas it is only of $\sim 1.6 \cdot 10^{-5} \text{ mmol} \cdot \text{m}^{-2} \cdot \text{d}^{-1}$ in the background GoM. This also
656 explains why, on average, the density/nitrate relation differs in the LCEs core (Fig 5.e). In response, the
657 $[\text{NO}_3]$ tendency due to biogeochemical processes indicates an increase of the $[\text{NO}_3]$ uptake. This
658 increase is about 1.5 times larger in the core ($\sim - 1.3 \cdot 10^{-3} \text{ mmol} \cdot \text{m}^{-2} \cdot \text{d}^{-1}$ integrated over the mixed layer)
659 than in the background GoM ($\sim - 0.9 \cdot 10^{-3} \text{ mmol} \cdot \text{m}^{-2} \cdot \text{d}^{-1}$). Knowing that it feeds biomass production, this
660 $[\text{NO}_3]$ loss is consistent with the primary production peak in winter (Fig 9.e and 9.f).

661
662 In summer, $[\text{NO}_3]$ variations due to vertical processes are smaller than in winter. They are also
663 weaker in the LCEs core upper layer (almost nil in the 0-50m layer) compared to the background GoM,
664 consistent with a deeper NO_3 pool and a shallow mixer layer. In the eddy core, one can assume that the
665 NO_3 vertical supply is entirely consumed before reaching 50m. Below 50m, vertical $[\text{NO}_3]$ diffusive
666 trends are consistently more important in the background GoM, in agreement with a steeper nitracline
667 (Fig 5.e). In contrast, vertical $[\text{NO}_3]$ advective trends in the eddy core are similar to or can eventually

668 exceed the trends in the background GoM (as in September and October for example). This confirms a
 669 pumping mechanism to sustain primary production in summer within the eddy core (section V.4) The
 670 biogeochemical activity related to $[\text{NO}_3]$ variations is also less intense in summer compared to winter.
 671 The depth of maximum $[\text{NO}_3]$ uptake is located just above the DCM and $[\text{NO}_3]$ release below. The loss
 672 of $[\text{NO}_3]$ is about twice larger in the background GoM ($\sim -0.9 \cdot 10^{-7} \text{ mmol} \cdot \text{m}^{-3} \cdot \text{d}^{-1}$) than in the LCEs core
 673 ($\sim -0.5 \cdot 10^{-7} \text{ mmol} \cdot \text{m}^{-3} \cdot \text{d}^{-1}$). It is noteworthy that the biogeochemical $[\text{NO}_3]$ source term, namely the
 674 nitrification rate, is really low within the eddy core.

675 To close this analysis of the $[\text{NO}_3]$ budget, it must be said that lateral diffusion and Asselin
 676 tendencies are marginal terms compared to the others. Horizontal advection is of the same order of
 677 magnitude as the vertical terms and mainly acts to redistribute horizontally the NO_3 vertically moved
 678 (see supplementary material 1).



679 **Figure B1: Seasonal cycle of nitrate trend terms in the (left column) LCEs core and in the (right column) background GoM. The**
 680 **trend induced by (a and b) vertical mixing, the (c and d) vertical advection and the (e and f) biogeochemical source minus sink are**
 681 **represented. Isopycnals anomalies (gray contours) and the depth of the mixed layer (black line) are superimposed.**

682 **REFERENCES:**

683 Ascani, F., Richards, K. J., Firing, E., Grant, S., Johnson, K. S., Jia, Y., et al. (2013). Physical and
684 biological controls of nitrate concentrations in the upper subtropical North Pacific Ocean. *Deep Sea*
685 *Research, Part II*, 93, 119–134.

686 Aumont, O., & Bopp, L. (2006). Globalizing results from ocean in situ iron fertilization studies. *Global*
687 *Biogeochemical Cycles*, 20, GB2017. <https://doi.org/10.1029/2005GB002591>.

688 Aumont, O., Ethé, C., Tagliabue, A., Bopp, L., & Gehlen, M. (2015). PISCES-v2: An ocean
689 biogeochemical model for carbon and ecosystem studies. *Geoscientific Model Development*, 8(8),
690 2465–2513.

691 Badan Jr, A., Candela, J., Sheinbaum, J., & Ochoa, J. (2005). Upper-layer circulation in the approaches
692 to Yucatan Channel. *Washington DC American Geophysical Union Geophysical Monograph*
693 *Series*, 161, 57-69.

694 Barnett, T. P., Pierce, D. W., & Schnur, R. (2001). Detection of anthropogenic climate change in the
695 world's oceans. *Science*, 292(5515), 270-274.

696 Behrenfeld, M. J., O'Malley, R. T., Siegel, D. A., McClain, C. R., Sarmiento, J. L., Feldman, G. C., ...
697 & Boss, E. S. (2006). Climate-driven trends in contemporary ocean productivity. *Nature*, 444(7120),
698 752.

699 Benitez-Nelson, C. R., Bidigare, R. R., Dickey, T. D., Landry, M. R., Leonard, C. L., Brown, S. L., ...
700 & Bibby, T. S. (2007). Mesoscale eddies drive increased silica export in the subtropical Pacific Ocean.
701 *Science*, 316(5827), 1017-1021.

702 Biggs, D. C., & Ressler, P. H. (2001). Distribution and abundance of phytoplankton, zooplankton,
703 ichthyoplankton, and micronekton in the deepwater Gulf of Mexico. *Gulf of Mexico Science*, 19(1), 2.

704 Bracco, A., Provenzale, A., & Scheuring, I. (2000). Mesoscale vortices and the paradox of the
705 plankton. *Proceedings of the Royal Society of London B: Biological Sciences*, 267(1454), 1795-1800.

706 Brodeau, L., Barnier, B., Treguier, A.-M., Penduff, T., & Gulev, S. (2010). An ERA40-based
707 atmospheric forcing for global ocean circulation models. *Ocean Modelling*, 31, 88–104. [https://doi.org/](https://doi.org/10.1016/j.ocemod.2009.10.005)
708 [10.1016/j.ocemod.2009.10.005](https://doi.org/10.1016/j.ocemod.2009.10.005)

709 Brokaw, R. J., Subrahmanyam, B., & Morey, S. L. (2019), Loop current and eddy driven salinity
710 variability in the Gulf of Mexico, *Geophysical Research Letters*, 46, 5978–5986,
711 <https://doi.org/10.1029/2019GL082931>.

712 Chelton, D., DeSzoek, R., Schlax, M., El Naggar, K., & Siwertz, N. (1998). Geographical variability
713 of the first baroclinic Rossby radius of deformation. *Journal of Physical Oceanography*, 28(3), 433–
714 460.

715 Ciani, D., Carton, X., Aguiar, A. B., Peliz, A., Bashmachnikov, I., Ienna, F., ... & Santoleri, R. (2017).
716 Surface signature of Mediterranean water eddies in a long-term high-resolution simulation. *Deep Sea*
717 *Research Part I: Oceanographic Research Papers*, 130, 12-29.

718 Cooper, C., Forristall, G. Z., & Joyce, T. M. (1990). Velocity and hydrographic structure of two Gulf of
 719 Mexico warm-core rings. *Journal of Geophysical Research: Oceans*, 95(C2), 1663-1679.

720 Cullen, J. J. (1982). The deep chlorophyll maximum: Comparing vertical profiles of chlorophyll a.
 721 Canadian Journal of Fisheries and Aquatic Sciences, 39(5), 791–803.

722 Dai, A., & Trenberth, K. E. (2002). Estimates of freshwater discharge from continents: Latitudinal and
 723 seasonal variations. *Journal of Hydro-meteorology*, 3, 660–687.

724 Damien, P., Pasqueron de Fommervault, O., Sheinbaum, J., Jouanno, J., Camacho-Ibar, V. F., &
 725 Duteil, O. (2018). Partitioning of the Open Waters of the Gulf of Mexico Based on the Seasonal and
 726 Interannual Variability of Chlorophyll Concentration. *Journal of Geophysical Research: Oceans*.

727 Danioux, E., Klein, P., & Rivière, P. (2008). Propagation of wind energy into the deep ocean through a
 728 fully turbulent mesoscale eddy field. *Journal of Physical Oceanography*, 38(10), 2224-2241.

729 Dewar, W., and G. Flierl (1987), Some effects of the wind on rings, *J. Phys. Oceanogr.*, 17(10), 1653–
 730 1667.

731 Doney, S. C., Glover, D. M., McCue, S. J., & Fuentes, M. (2003). Mesoscale variability of Sea-viewing
 732 Wide Field-of-view Sensor (SeaWiFS) satellite ocean color: Global patterns and spatial scales. *Journal*
 733 *of Geophysical Research: Oceans*, 108(C2).

734 Dong, C., X. Lin, Y. Liu, F. Nencioli, Y. Chao, Y. Guan, D. Chen, T. Dickey, and J. C. McWilliams
 735 (2012), Three-dimensional oceanic eddy analysis in the Southern California Bight from a numerical
 736 product, *J. Geophys. Res.*, 117, C00H14, doi:10.1029/2011JC007354.

737 Donohue, Kathleen A., et al. "Loop current eddy formation and baroclinic instability." *Dynamics of*
 738 *Atmospheres and Oceans* 76 (2016): 195-216.

739 d'Ovidio, F., De Monte, S., Della Penna, A., Cotté, C., & Guinet, C. (2013). Ecological implications of
 740 eddy retention in the open ocean: a Lagrangian approach. *Journal of Physics A: Mathematical and*
 741 *Theoretical*, 46(25), 254023.

742 Dufois, F., Hardman-Mountford, N. J., Greenwood, J., Richardson, A. J., Feng, M., Herbette, S., &
 743 Matear, R. (2014). Impact of eddies on surface chlorophyll in the South Indian Ocean. *Journal of*
 744 *Geophysical Research: Oceans*, 119(11), 8061-8077.

745 Dufois, F., Hardman-Mountford, N. J., Greenwood, J., Richardson, A. J., Feng, M., & Matear, R. J.
 746 (2016). Anticyclonic eddies are more productive than cyclonic eddies in subtropical gyres because of
 747 winter mixing. *Science advances*, 2(5), e1600282.

748 Dufois, F., Hardman-Mountford, N. J., Fernandes, M., Wojtasiewicz, B., Shenoy, D., Slawinski, D., ...
 749 & Toresen, R. (2017). Observational insights into chlorophyll distributions of subtropical South Indian
 750 Ocean eddies. *Geophysical Research Letters*, 44(7), 3255-3264.

751 Dugdale, R. C., and J. J. Goering (1967), Uptake of new and regenerated forms of nitrogen in primary
 752 productivity, *Limnol. Oceanogr.*, 12, 196–206

753 Early, J. J., Samelson, R. M., & Chelton, D. B. (2011). The evolution and propagation of
754 quasigeostrophic ocean eddies. *Journal of Physical Oceanography*, 41(8), 1535-1555.

755 Elliott, B. A. (1982). Anticyclonic rings in the Gulf of Mexico. *Journal of Physical Oceanography*,
756 12(11), 1292-1309.

757 Eppley, R. W., and B. J. Peterson (1979), Particulate organic matter flux and planktonic new
758 production in the deep ocean, *Nature*, 282, 677–680.

759 Falkowski, P., D. Ziemann, Z. Kolber, and P. Bienfang (1991), Role of eddy pumping in enhancing
760 primary production in the ocean, *Nature*, 352(6330), 55–58.

761 Flierl, G. R. (1981). Particle motions in large-amplitude wave fields. *Geophysical & Astrophysical*
762 *Fluid Dynamics*, 18(1-2), 39-74.

763 Flierl, G. R., & McGillicuddy, D. J. (2002). Mesoscale and submesoscale physical-biological
764 interactions. *The sea*, 12, 113-185.

765 de Fommervault, O. P., Perez-Brunius, P., Damien, P., Camacho-Ibar, V. F., & Sheinbaum, J. (2017).
766 Temporal variability of chlorophyll distribution in the Gulf of Mexico: bio-optical data from profiling
767 floats. *Biogeosciences*, 14(24), 5647.

768 Forristall, G. Z., Schaudt, K. J., & Cooper, C. K. (1992). Evolution and kinematics of a Loop Current
769 eddy in the Gulf of Mexico during 1985. *Journal of Geophysical Research: Oceans*, 97(C2), 2173-
770 2184.

771 Frolov, S. A., et al. "Loop Current eddy interaction with the western boundary in the Gulf of Mexico."
772 *Journal of physical oceanography* 34.10 (2004): 2223-2237.

773 Garcia-Jove Navarro, M., Sheinbaum Pardo, J., & Jouanno, J. (2016). Sensitivity of Loop Current
774 metrics and eddy detachments to different model configurations: The impact of topography and
775 Caribbean perturbations. *Atmosfera*, 29(3), 235–265. <https://doi.org/10.20937/ATM.2016.29.03.05>

776 Garçon, V. C., Oschlies, A., Doney, S. C., McGillicuddy, D., & Waniek, J. (2001). The role of
777 mesoscale variability on plankton dynamics in the North Atlantic. *Deep Sea Research Part II: Topical*
778 *Studies in Oceanography*, 48(10), 2199-2226.

779 Gaube, P., Chelton, D. B., Strutton, P. G., & Behrenfeld, M. J. (2013). Satellite observations of
780 chlorophyll, phytoplankton biomass, and Ekman pumping in nonlinear mesoscale eddies. *Journal of*
781 *Geophysical Research: Oceans*, 118(12), 6349-6370.

782 Gaube, P., McGillicuddy, D. J., Chelton, D. B., Behrenfeld, M. J., & Strutton, P. G. (2014). Regional
783 variations in the influence of mesoscale eddies on near-surface chlorophyll. *Journal of Geophysical*
784 *Research: Oceans*, 119(12), 8195-8220.

785 Gaube, P., Chelton, D. B., Samelson, R. M., Schlax, M. G., & O'Neill, L. W. (2015). Satellite
786 observations of mesoscale eddy-induced Ekman pumping. *Journal of Physical Oceanography*, 45(1),
787 104-132.

788 Geider, R. J. (1987), Light and temperature dependence of the carbon to chlorophyll a ratio in
789 microalgae and cyanobacteria: implications for physiology and growth of phytoplankton, *New Phytol.*,
790 106, 1–34.

791 Geider, R. J., MacIntyre, H. L., & Kana, T. M. (1997). A dynamical model of phytoplankton growth
792 and acclimation: Response of the balanced growth rate to light, nutrient limitation and temperature.
793 *Marine Ecology Progress Series*, 148, 187–200.

794 Glenn, S. M., and C. C. Ebbesmeyer (1993), Drifting buoy observations of a loop current
795 anticyclonic eddy, *J. Geophys. Res.*, , 98, 20, doi:10.1029/93JC02078.

796 Green, R. E., Bower, A. S., & Lugo-Fernández, A. (2014). First autonomous bio-optical profiling float
797 in the Gulf of Mexico reveals dynamic biogeochemistry in deep waters. *PloS one*, 9(7), e101658.

798 Guo, M., P. Xiu, S. Li, F. Chai, H. Xue, K. Zhou, and M. Dai (2017), Seasonal variability and
799 mechanisms regulating chlorophyll distribution in mesoscale eddies in the South China Sea, *J.*
800 *Geophys. Res. Oceans*, 122, 5329–5347, doi:10.1002/2016JC012670.

801 Hamilton, P., Leben, R., Bower, A., Furey, H., & Pérez-Brunius, P. (2018). Hydrography of the Gulf of
802 Mexico Using Autonomous Floats. *Journal of Physical Oceanography*, 48(4), 773-794. DOI: 10.1175/
803 JPO-D-17-0205.1

804 Hamilton, P. (2007). Eddy statistics from Lagrangian drifters and hydrography for the northern Gulf of
805 Mexico slope. *Journal of Geophysical Research*, 112, C09002. <https://doi.org/10.1029/2006JC003988>

806 He, Q., Zhan, H., Shuai, Y., Cai, S., Li, Q. P., Huang, G., & Li, J. (2017). Phytoplankton bloom
807 triggered by an anticyclonic eddy: The combined effect of eddy Ekman pumping and winter mixing.
808 *Journal of Geophysical Research: Oceans*, 122(6), 4886-4901.

809 Hernandez-Guerra, A., & Joyce, T. M. (2000). Water masses and circulation in the surface layers of the
810 Caribbean at 66 W. *Geophysical Research Letters*, 27(21), 3497–3500.
811 <https://doi.org/10.1029/1999GL011230>

812 Herrmann, M., Somot, S., Sevault, F., Estournel, C., & Deque, M. (2008). Modeling the deep
813 convection in the northwestern Mediterranean Sea using an eddy-permitting and an eddy-resolving
814 model: Case study of winter 1986–1987. *Journal of Geophysical Research*, 113, C04011.
815 <https://doi.org/10.1029/2006JC003991>

816 Huang, J., & Xu, F. (2018). Observational evidence of subsurface chlorophyll response to mesoscale
817 eddies in the North Pacific. *Geophysical Research Letters*, 45, 8462–8470.
818 <https://doi.org/10.1029/2018GL078408>

819 Jolliff, J. K., Kindle, J. C., Penta, B., Helber, R., Lee, Z., Shulman, I., Arnone, R., and Rowley, C. D.,
820 (2008). On the relationship between satellite-estimated bio-optical and thermal properties in the Gulf of
821 Mexico, *J. Geophys. Res.*, 113, G1, <https://doi.org/10.1029/2006JG000373>

822 Jouanno, J., Ochoa de la Torre, J. L., Pallas Sanz, E., Sheinbaum Pardo, J., Andrade Canto, F., Candela
 823 Perez, J., et al. (2016). Loop current frontal eddies: Formation along the Campeche Bank and impact of
 824 coastally trapped waves. *Journal of Physical Oceanography*, 46(11), 3339–3363.
 825 <https://doi.org/10.1175/JPO-D-16-0052.1>

826 Klein, P., & Lapeyre, G. (2009). The oceanic vertical pump induced by mesoscale and submesoscale
 827 turbulence. *Annual review of marine science*, 1, 351-375.

828 Koszalka, I. M., Ceballos, L., & Bracco, A. (2010). Vertical mixing and coherent anticyclones in the
 829 ocean: the role of stratification. *Nonlinear Processes in Geophysics*, 17(1), 37-47.

830 Kouketsu, S., Tomita, H., Oka, E., Hosoda, S., Kobayashi, T., & Sato, K. (2011). The role of meso-
 831 scale eddies in mixed layer deepening and mode water formation in the western North Pacific. In *New*
 832 *Developments in Mode-Water Research* (pp. 59-73). Springer, Tokyo.

833 Kunze, E. (1985). Near-inertial wave propagation in geostrophic shear. *Journal of Physical*
 834 *Oceanography*, 15(5), 544-565.

835 Lascaratos, A., & Nittis, K. (1998). A high-resolution three-dimensional numerical study of
 836 intermediate water formation in the Levantine Sea. *Journal of Geophysical Research*, 103(C9), 18497–
 837 18511.

838 Lehahn, Y., F. d'Ovidio, M. Levy, Y. Amitai, and E. Heifetz (2011), Long range transport of a quasi
 839 isolated chlorophyll patch by an Agulhas ring, *Geophys. Res. Lett.*, 38, L16610,
 840 [doi:10.1029/2011GL048588](https://doi.org/10.1029/2011GL048588).

841 Le Hénaff, M., Kourafalou, V. H., Morel, Y., & Srinivasan, A. (2012). Simulating the dynamics and
842 intensification of cyclonic Loop Current Frontal Eddies in the Gulf of Mexico. *Journal of Geophysical*
843 *Research: Oceans*, 117(C2).

844 Levitus, S. (1982). Climatological atlas of the world ocean (NOAA Prof. Pap. 13, 173 p.). Washington,
845 DC: U.S. Government Printing Office.

846 Lévy, M., Ferrari, R., Franks, P. J., Martin, A. P., & Rivière, P. (2012). Bringing physics to life at the
847 submesoscale. *Geophysical Research Letters*, 39(14).

848 Lévy, M., Franks, P.J.S. & Smith, K.S. (2018). The role of submesoscale currents in structuring marine
849 ecosystems. *Nat. Commun.*, **9**, 4758

850 Linacre, L., Lara-Lara, R., Camacho-Ibar, V., Herguera, J. C., Bazán-Guzmán, C., & Ferreira-Bartrina,
851 V. (2015). Distribution pattern of picoplankton carbon biomass linked to mesoscale dynamics in the
852 southern gulf of Mexico during winter conditions. *Deep Sea Research Part I: Oceanographic Research*
853 *Papers*, 106, 55-67.

854 Linacre, L., Durazo, R., Camacho-Ibar, V. F., Selph, K. E., Lara-Lara, J. R., Mirabal-Gómez, U., ... &
855 Sidón-Ceseña, K. (2019). Picoplankton Carbon Biomass Assessments and Distribution of
856 *Prochlorococcus* Ecotypes Linked to Loop Current Eddies During Summer in the Southern Gulf of
857 Mexico. *Journal of Geophysical Research: Oceans*, 124(11), 8342-8359.

858 Lipphardt, B., Poje, A. C., Kirwan, A., Kantha, L., & Zweng, M. (2008). Death of three Loop Current
859 rings. *Journal of Marine Research*, 66(1), 25-60.

860 Madec, G. (2016). NEMO ocean engine, Note Du Pole De Mod# elisation (Vol. 27, 406 p.). Paris,
861 France: Institut Pierre-Simon Laplace.

862 Mann, K. H., & Lazier, J. R. N. (2006). Dynamics of marine ecosystems (3rd ed.). Oxford, UK:
863 Blackwell Publishing.

864 Mahadevan, A. (2014). Ocean science: Eddy effects on biogeochemistry. *Nature*, 506(7487), 168.

865 Martin, A. P., & Richards, K. J. (2001). Mechanisms for vertical nutrient transport within a North
866 Atlantic mesoscale eddy. *Deep Sea Research Part II: Topical Studies in Oceanography*, 48(4-5), 757-
867 773.

868 Mayot, N., D'Ortenzio, F., Taillandier, V., Prieur, L., de Fommervault, O. P., Claustre, H., ... & Conan,
869 P. (2017). Physical and biogeochemical controls of the phytoplankton blooms in North Western
870 Mediterranean Sea: A multiplatform approach over a complete annual cycle (2012–2013 DEWEX
871 experiment). *Journal of Geophysical Research: Oceans*, 122(12), 9999-10019.

872 McClain, C. R., Signorini, S. R., & Christian, J. R. (2004). Subtropical gyre variability observed by
873 ocean-color satellites. *Deep Sea Research Part II: Topical Studies in Oceanography*, 51(1-3), 281-301.

874 McGillicuddy, D. J., Jr. (2016), Mechanisms of Physical-Biological-Biogeochemical Interaction at the
875 Oceanic Mesoscale, *Annu. Rev. Mar. Sci.*, 8, 125–159, doi:10.1146/annurev-marine-010814-015606.

876 McGillicuddy Jr, D. J., Robinson, A. R., Siegel, D. A., Jannasch, H. W., Johnson, R., Dickey, T. D., ...
877 & Knap, A. H. (1998). Influence of mesoscale eddies on new production in the Sargasso Sea. *Nature*,
878 394(6690), 263.

879 McGillicuddy Jr, D. J., & Robinson, A. R. (1997). Eddy-induced nutrient supply and new production in
880 the Sargasso Sea. *Deep Sea Research Part I: Oceanographic Research Papers*, 44(8), 1427-1450.

881 Meunier, T., Sheinbaum, J., Pallàs-Sanz, E., Tenreiro, M., Ochoa, J., Ruiz-Angulo, A., ... & de Marez,
882 C. (2020). Heat Content Anomaly and Decay of Warm-Core Rings: the Case of the Gulf of Mexico.
883 *Geophysical Research Letters*, 47(3), e2019GL085600.

884 Meunier, T., Tenreiro, M., Pallàs-Sanz, E., Ochoa, J., Ruiz-Angulo, A., Portela, E., et al. (2018a).
885 Intrathermocline eddies embedded within an anticyclonic vortex ring. *Geophysical Research Letters*,
886 45. <https://doi.org/10.1029/2018GL077527>

887 Meunier, T., Pallàs-Sanz, E., Tenreiro, M., Rodriguez, E. P., Ochoa, J., Ruiz-Angulo, A., & Cusí, S.
888 (2018b). The Vertical structure of a Loop Current Eddy. *Journal of Geophysical Research: Oceans*.

889 Mignot, A., Claustre, H., Uitz, J., Poteau, A., D'Ortenzio, F., and Xing, X., (2014), Understanding the
890 seasonal dynamics of phytoplankton biomass and the deep chlorophyll maximum in oligotrophic
891 environments: A Bio-Argo float investigation, *Global Biogeochem. Cy.*, 28, 856–876.

892 Monterey, G., & Levitus, S. (1997). Seasonal variability of mixed layer depth for the World Ocean
 893 (NOAA Atlas NESDIS 14, 100 p.). Silver Spring, MD: National Oceanic and Atmospheric
 894 Administration.

895 Muller-Karger, F. E., Walsh, J. J., Evans, R. H., & Meyers, M. B. (1991). On the seasonal
 896 phytoplankton concentration and sea surface temperature cycles of the Gulf of Mexico as determined
 897 by satellites. *Journal of Geophysical Research*, 96(C7), 12645–12665.

898 Myers, V. B., & Iverson, R. I. (1981). Phosphorus and nitrogen limited phytoplankton productivity in
 899 northeastern Gulf of Mexico coastal estuaries. In *Estuaries and nutrients* (pp. 569-582). Humana Press.

900 Nencioli, F., C. Dong, T. Dickey, L. Washburn, and J. C. McWilliams (2010), A vector geometry-
 901 based eddy detection algorithm and its application to a high-resolution numerical model product and
 902 high-frequency radar surface velocities in the Southern California Bight, *J. Atmos. Oceanic Technol.*,
 903 27, 564–579, doi:10.1175/2009JTECHO725.1.

904 Nof, D., 1981: On the b-induced movement of isolated baroclinic eddies. *J. Phys. Oceanogr.*, 11, 1662–
 905 1672, [https://doi.org/ 10.1175/1520-0485\(1981\)011,1662:OTIMOI.2.0.CO;2](https://doi.org/10.1175/1520-0485(1981)011<1662:OTIMOI.2.0.CO;2).

906 Nowlin, W. D. Jr., & Parker, C. A. (1974). Effects of a cold-air outbreak on shelf waters of the Gulf of
 907 Mexico. *Journal of Physical Oceanography*, 4(3), 467–486.

908 Omand, M. M., D’Asaro, E. A., Lee, C. M., Perry, M. J., Briggs, N., Cetinić, I., & Mahadevan, A.
 909 (2015). Eddy-driven subduction exports particulate organic carbon from the spring bloom. *Science*,
 910 348(6231), 222-225.

911 Omand, M. M., & Mahadevan, A. (2014). Shape of the oceanic nitracline. *Biogeosciences Discussions*,
912 11, 14729–14763.

913 Oschlies, A., & Garcon, V. (1998). Eddy-induced enhancement of primary production in a model of the
914 North Atlantic Ocean. *Nature*, 394(6690), 266.

915 Pallàs-Sanz, E., Candela, J., Sheinbaum, J., Ochoa, J., & Jouanno, J. (2016). Trapping of the near-
916 inertial wave wakes of two consecutive hurricanes in the Loop Current. *Journal of Geophysical*
917 *Research: Oceans*, 121(10), 7431-7454.

918 Passalacqua, G. A., Sheinbaum, J., & Martinez, J. A. (2016). Sea surface temperature influence on a
919 winter cold front position and propagation: Air-sea interactions of the ‘Nortes’ winds in the Gulf of
920 Mexico. *Atmospheric Science Letters*, 17(5), 302–307.

921 Polovina, J. J., Howell, E. A., & Abecassis, M. (2008). Ocean's least productive waters are expanding.
922 *Geophysical Research Letters*, 35(3).

923 Sathyendranath, S, Brewin, RJW, Müeller, D, Brockmann, C, Deschamps, P-Y, Doerffer, R, Fomferra,
924 N, Franz, BA, Grant, MG, Hu C, Krasemann, H, Lee, Z, Maritorena, S, Devred, E, Mélin, F, Peters, M,
925 Smyth, T, Steinmetz, F, Swinton, J, Werdell, J, Regner, P (2012) Ocean Colour Climate Change
926 Initiative: Approach and Initial Results, IGARSS 2012, 2024-2027.
927 doi:10.1109/IGARSS.2012.6350979.

928 Sheinbaum Pardo, J., Athie De Velasco, G. E., Candela Perez, J., Ochoa de la Torre, J. L., & Romero
 929 Arteaga, A. M. (2016). Structure and variability of the Yucatan and loop currents along the slope and
 930 shelf break of the Yucatan channel and Campeche bank. *Dynamics of Atmospheres and Oceans*, 76,
 931 217–239. <https://doi.org/10.1016/j.dynatmoce.2016.08.001>

932 Sherr, E. B., & Sherr, B. F. (2002). Significance of predation by protists in aquatic microbial food
 933 webs. *Antonie van Leeuwenhoek*, 81(1), 293-308.

934 Siegel, D. A., Behrenfeld, M. J., Maritorena, S., McClain, C. R., Antoine, D., Bailey, S. W., ... & Eplee
 935 Jr, R. E. (2013). Regional to global assessments of phytoplankton dynamics from the SeaWiFS
 936 mission. *Remote Sensing of Environment*, 135, 77-91.

937 Siegel, D. A., McGillicuddy Jr, D. J., & Fields, E. A. (1999). Mesoscale eddies, satellite altimetry, and
 938 new production in the Sargasso Sea. *Journal of Geophysical Research: Oceans*, 104(C6), 13359-
 939 13379.

940 Sosa-Gutiérrez, R., et al. "Erosion of the Subsurface Salinity Maximum of the Loop Current Eddies
 941 From Glider Observations and a Numerical Model." *Journal of Geophysical Research: Oceans* 125.7
 942 (2020): e2019JC015397.

943 Strickland, J. D. H. (1965). Production of organic matter in the primary stages of the marine food
 944 chain, *Chem. Oceanogr.*, 1, 477–610.

945 Sturges, W., & Leben, R. (2000). Frequency of ring separations from the Loop Current in the Gulf of
 946 Mexico: A revised estimate. *Journal of Physical Oceanography*, 30, 1814–1819.

947 Sturges, W., & Kenyon, K. E. (2008). Mean flow in the Gulf of Mexico. *Journal of Physical*
948 *Oceanography*, 38(7), 1501-1514.

949 Sweeney, E. N., D. J. McGillicuddy, and K. O. Buesseler (2003), Biogeochemical impacts due to
950 mesoscale eddy activity in the Sargasso Sea as measured at the Bermuda Atlantic Time-series Study
951 (BATS), *Deep Sea Res., Part II*, 50(22–26), 3017–3039, doi:10.1016/j.dsr2.2003.07.008.

952 Tenreiro, M., Candela, J., Sanz, E. P., Sheinbaum, J., & Ochoa, J. (2018). Near-Surface and Deep
953 Circulation Coupling in the Western Gulf of Mexico. *Journal of Physical Oceanography*, 48(1), 145-
954 161.

955 Travis, S., & Qiu, B. (2020). Seasonal Reversal of the Near-Surface Chlorophyll Response to the
956 Presence of Mesoscale Eddies in the South Pacific Subtropical Countercurrent. *Journal of Geophysical*
957 *Research: Oceans*, 125(3), e2019JC015752.

958 Turner, J. S. (1973). Buoyancy effects in fluids (368 p.). New York, NY: Cambridge University Press.

959 Turner, R. E., Rabalais, N. N., & Justic, D. (2006). Predicting summer hypoxia in the northern Gulf of
960 Mexico: Riverine N, P, and Si loading. *Marine pollution bulletin*, 52(2), 139-148.

961 Vukovich, F. M., 2007: Climatology of ocean features in the Gulf of Mexico using satellite remote
962 sensing data. *J. Phys. Oceanogr.*, 37, 689–707, <https://doi.org/10.1175/JPO2989.1>.

963 Waite, A. M., S. Pesant, D. A. Griffin, P. A. Thompson, and C. M. Holl (2007), *Oceanography*,
 964 primary production and dissolved inorganic nitrogen uptake in two Leeuwin Current eddies, *Deep Sea*
 965 *Res., Part II*, 54(8–10), 981–1002, doi:10.1016/j.dsr2.2007.03.001.

966 Wawrik, B., Paul, J., Bronk, D., John, D., Gray, M., 2004. High rates of ammonium recycling drive
 967 phytoplankton productivity in the offshore Mississippi River plume. *Aquat. Microb. Ecol.* 35, 175–184.
 968 <http://dx.doi.org/10.3354/ame035175>.

969 Weisberg, R. H., & Liu, Y. (2017). On the Loop Current penetration into the Gulf of Mexico. *Journal*
 970 *of Geophysical Research: Oceans*, 122(12), 9679–9694.

971 Williams, R. G. (1988). Modification of ocean eddies by air-sea interaction. *Journal of Geophysical*
 972 *Research: Oceans*, 93(C12), 15523–15533.

973 Wu, G. (1964). Stratification and circulation in the Antillean-Caribbean basins (Vol. 1). New York,
 974 NY: Columbia University Press.

975 Zhao, J., Bower, A., Yang, J., & Lin, X. (2018). Meridional heat transport variability induced by
 976 mesoscale processes in the subpolar North Atlantic. *Nature communications*, 9(1), 1124.

977 Zhong, Y., & Bracco, A. (2013). Submesoscale impacts on horizontal and vertical transport in the Gulf
 978 of Mexico, *Journal of Geophysical Research: Oceans*, 118(10), 5651–5668.